LLE Review
Quarterly Report

June, 1980 - August, 1980

LLE Review
Quarterly Report

Editor: **R. L. McCrory**
(716-275-4973)

June, 1980 - August, 1980

UR
LLE

IN BRIEF

During the period from June through September, significant progress has been made in a number of areas. They include:

the activation of the OMEGA uniform illumination implosion facility,

diagnostic development for core density measurements in imploded targets,

theoretical determination of the gains to be made in target performance by conversion of the driver wavelength to $0.3513 \mu m$,

and new facility and instrumentation development in picosecond and subpicosecond research.

Highlights of these activities are:

● Initial alignment and focusing multi-beam target shots were conducted on the OMEGA system with the resulting x-ray pinhole camera images serving as the first target diagnostic for alignment and focusing accuracy. Pointing and focusing of all beams on target was well within the required specifications for the upcoming uniform implosion studies.

● Preliminary measurements of OMEGA beam propagation indicate that acceptable beam quality and focusing characteristics can be achieved at the target chamber.

- Numerical modeling of the impressed laser beam profiles at the absorption surface of the target has provided us with results that indicate uniformity in excess of 95% is achievable for spherical implosion experiments.

- X-ray spectroscopy of the compressed cores in the imploded targets has verified the higher predicted core densities with improved irradiation symmetry.

- Earlier estimates of improved target performance with a shorter wavelength laser driver have been refined by detailed calculations on the laser radiation absorption efficiency at $0.3513 \mu m$. These calculations support our earlier enthusiasm for higher target performance efficiency at shorter wavelength and provide the guidance for short wavelength interaction experiments to be carried out in the next quarter.

- The development, construction, and demonstration of a simple picosecond streak camera with subpicosecond jitter has been completed in this quarter.

CONTENTS

The cover photograph shows an engineer at the Laboratory for Laser Energetics aligning one of the injection mirrors in the OMEGA laser system. These mirrors direct the laser beams from the output of each beamline toward the final turning mirrors located in the target bay.

Section 1
PROGRESS ON OMEGA

1.A OMEGA Activation

The principal activity on OMEGA during the last quarter was the installation of components in the target area and the initiation of 2 and 6 beam target calibration shots. These experiments are designed to test the laser beam pointing and focusing on spherical microballoon targets with each of the 24 beams. The diagnostics employed for these tests consisted of two x-ray pinhole cameras to provide spatially resolved photographs of the x-ray emission from the target.

The OMEGA 24 beam neodymium phosphate glass laser system ($\lambda = 1.054\mu m$) performance tests were reported in a previous issue of the LLE Review (Volume 2). The OMEGA system design features allow the high repetition rate of one shot every 30 minutes at a power level of 12 TW for a pulse length of 50 psec.

Table 1

The principal objectives and results from the OMEGA laser system performance test.

|	Minimum DOE Requirements	Design Goal	OMEGA Output (1/80)
Peak Power (short pulse)	7.5 TW (50 psec)	12-14 TW (50 psec)	12.2 TW (53 psec)
Energy (long pulse)	1.2 kJ (300 psec)	2.5 kJ (300 psec)	1.76 kJ (273 psec)

The principal objectives and results from the performance tests are summarized in Table 1. Further details of these tests can be found in the LLE Review, Volume 2.

The OMEGA target area is shown in Figure 1; the large structure supports the final turning mirrors for directing 24 beams to the target chamber and focusing lenses. The activities during the last quarter consisted of assembly of components in the target area including optics, target chamber support equipment, and diagnostics. The following major components have been installed and tested:

1. All optical mirrors and covers were installed on the turning mirror structure.
2. 17 of the 24 single element f/3 focusing lenses were installed in the target chamber.
3. The target chamber vacuum system was tested and obtained a pressure of 5×10^{-7} torr.

Figure 1

Photograph of the OMEGA target area showing the turning mirror support structure and experimental chamber.
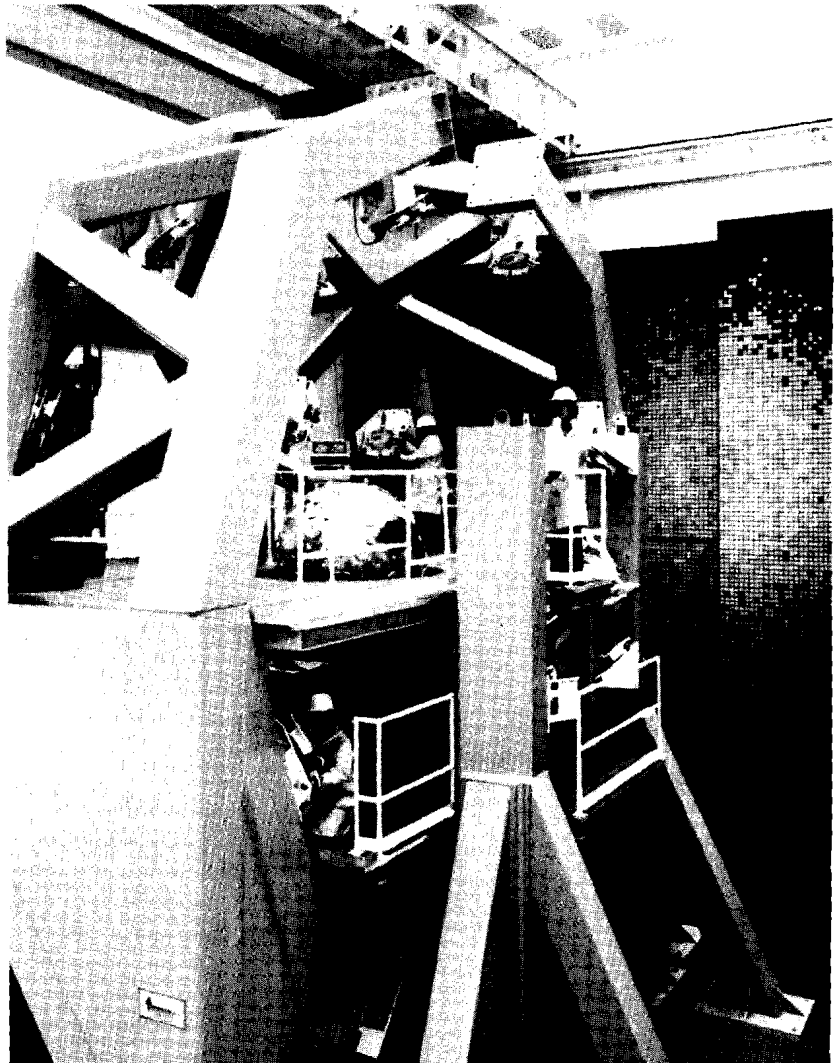
4. The target positioner, capable of holding up to 16 targets, was placed on the target chamber.
5. The target chamber viewing system, for positioning of targets, was installed.

Additional construction activities included the OMEGA diagnostic control room for data acquisition and the fabrication of diagnostic systems which included 20 plasma calorimeters for absorbed energy measurements, two x-ray pinhole cameras for spatial x-ray imaging, and neutron counters.

During the quarter, 17 target shots were taken on the OMEGA facility. These first series of target shots were designed to test the pointing, focusing, and timing of the OMEGA illumination system. The test results are obtained by irradiating an empty glass microballoon of 200 μm diameter and a 2.0 μm glass wall with two and six beams. X-ray images of the plasma emission are obtained from an x-ray pinhole camera and compared with the predicted results. A typical experiment with 2 beams focused on the target surface shows three well-defined x-ray images in a straight line; the outer images are the result of localized plasma heating from the focused beam energy; the center image is due to the two colliding glass segments stagnating at target center. Gross errors in beam timing are observed if the central x-ray image is displaced from target center. The location of beam focusing is compared with predicted results by similar experiments which translate the beam focus from inside to outside the target surface. This focusing change should result in a larger x-ray image than that obtained with a surface focus condition.

1.B OMEGA Beam Propagation

OMEGA utilizes the imaging property of its spatial filters to relay an image of a hard aperture, located at the output of the oscillator, through each of its amplifiers. This concept, first proposed by John Hunt at LLNL, allows the system to be operated at a high fill factor and minimizes diffraction effects that can lead to beam breakup and subsequent catastrophic damage of optical components in the system. The last image plane in OMEGA is located approximately 2 meters beyond the output spatial filter in each of the 24 beamlines. Each beam propagates from this plane to the target chamber focusing lens without additional spatial filtering or image relaying. The total unrelayed optical path for each beam is approximately 30 meters. The presence of this large unrelayed optical path has been a cause for concern regarding the beam quality at the focusing lens.

An additional cause for concern is the fact that the beams are unenclosed over the 30 meter path between the output of the
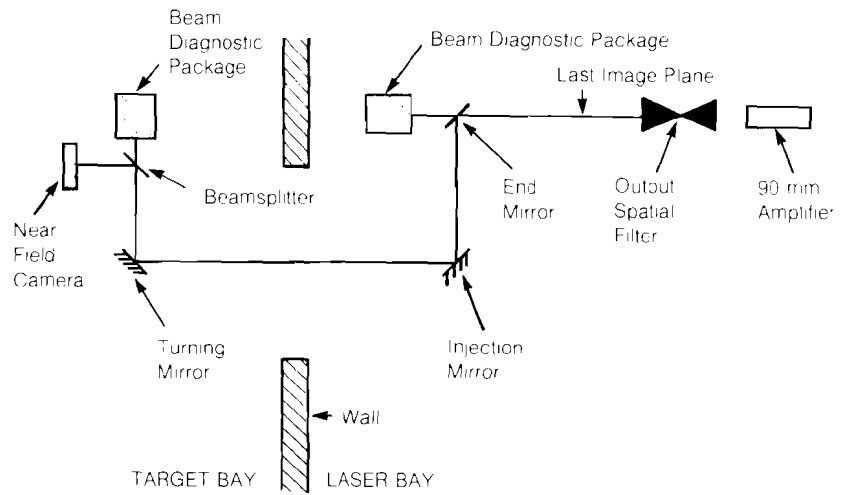
Figure 2
Laser beam path from system output.

Beam Diagnostic Package

Beam Diagnostic Package

Last Image Plane

Beamsplitter

Near Field Camera

End Mirror

Output Spatial Filter

90 mm Amplifier

Turning Mirror

Injection Mirror

← Wall

TARGET BAY   LASER BAY

laser system and the focusing lens. This has led to speculation that the beam quality would be substantially degraded by air turbulence in the laser and target bays. Experience at LLNL suggested that beam enclosures would be necessary; however, the air conditioning systems at the Shiva and OMEGA facilities are of considerably different design.

A preliminary series of experiments has been conducted to determine the magnitude of these potential problems. The problem of beam quality degradation was addressed by photographing the far field distribution of a single beam in the laser bay and near the target chamber using the standard OMEGA beam diagnostic package (BDP).
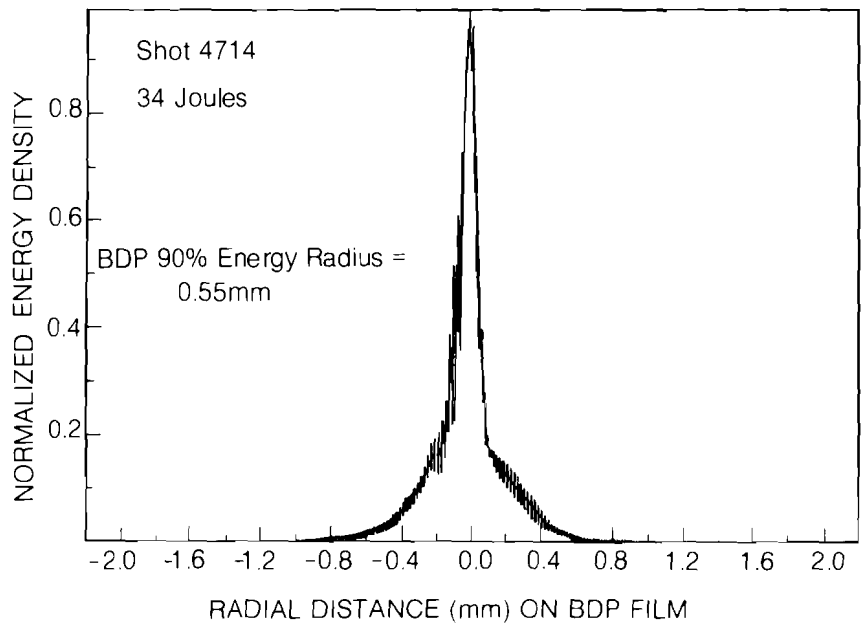
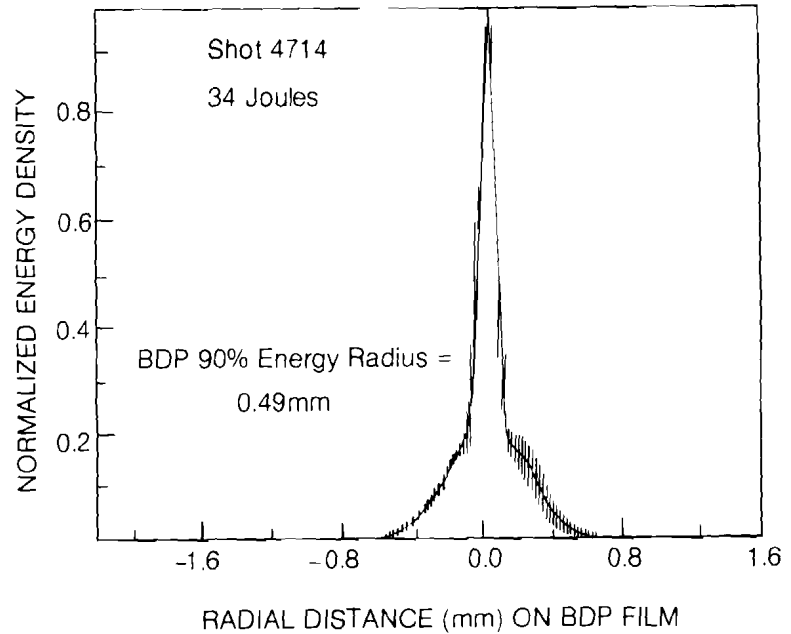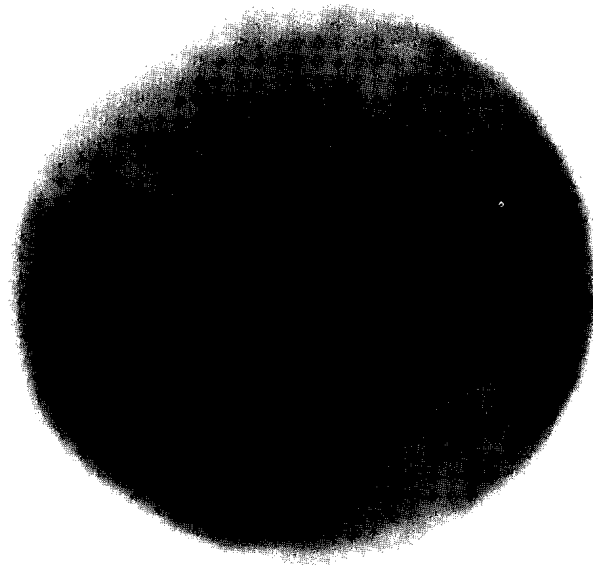Figure 3
Laser bay far field beam profile.

Shot 4714

34 Joules

BDP 90% Energy Radius = 0.55mm

NORMALIZED ENERGY DENSITY

RADIAL DISTANCE (mm) ON BDP FILM

Figure 4
Target bay far field beam profile.

The BDP uses a 4.5 meter focal length lens to produce a photograph of the beam at the equivalent target plane on 35mm film. Experience with ZETA has shown that there is a high correlation between the BDP equivalent target plane photographs and the x-ray emission as seen in pinhole camera photographs of gold coated targets. Thus, the BDP can be used as a diagnostic to determine on-target beam quality.
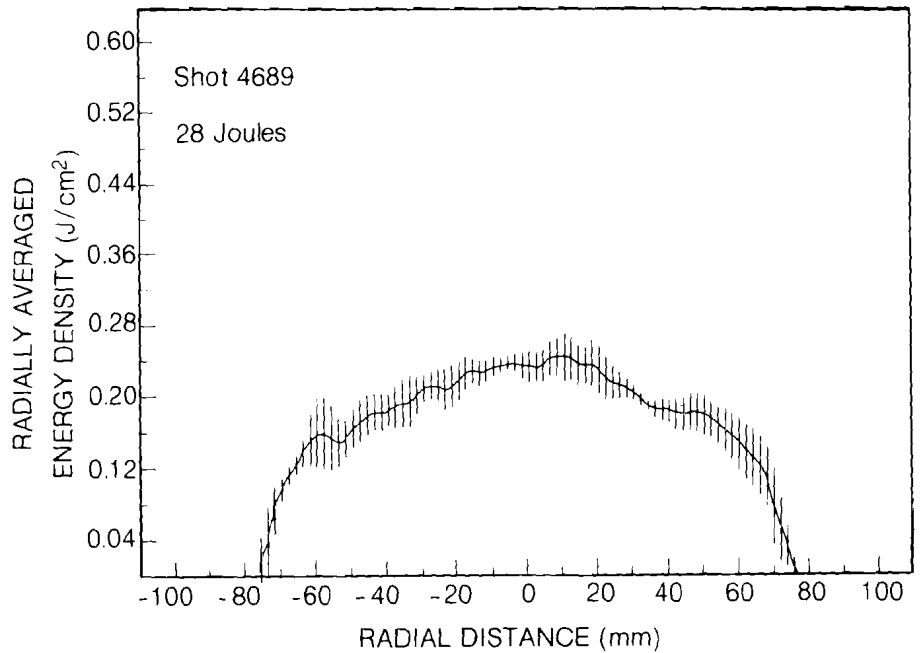
The problem of diffraction and beam breakup was addressed in a separate experiment using a near field photograph taken in a

Figure 5
Near field photograph of an OMEGA beam in the target bay.

Shot 4689

Figure 6
Target bay near field beam profile.

plane near the final focusing lens. Significant modulation of the beam intensity profile in this plane can result in damage of the focusing lens. Figure 2 illustrates the arrangement of equipment for each of these experiments.

Figure 3 shows the average of 4 radial scans of the far field photograph taken in the laser bay. Figure 4 shows the average of 4 radial scans of the far field photo taken in the target bay. Figure 5 is a near field photograph of the beam taken near the OMEGA chamber and Figure 6 is an average of four radial scans of the near field photo.

The following conclusions can be drawn from these photographs:

1. The similarity of the BDP far field photographs taken in the laser bay and the target bay indicates that there is no significant change in focusing characteristics due to air turbulence or the lack of image relaying over the 30 meter path.

2. The lack of significant modulation in the near field photograph in the target bay indicates that the beam arrives at the chamber without breaking-up despite the lack of image relaying, thus damage of the focusing optics is unlikely.

It should be emphasized that these are preliminary measurements, and additional experiments are planned in an effort to further understand the propagation of these high energy beams. These experiments will be useful in normalizing propagation codes, which will then be used to enhance the performance of OMEGA.

1.C Uniformity of Illumination Studies for OMEGA

Arranging the distribution of irradiation on the surface of spherical targets as uniformly as possible is an important goal for laser

fusion. A multi-beam symmetric irradiation capability is one of the distinct features of the OMEGA facility. It is expected that the more uniform the distribution of irradiation, the more uniform will be the temperature on the target surface, resulting in higher compression and implosion quality.

We summarize our present results from studies of the achievable uniformity to be expected on OMEGA.

In principle, and under ideal situations, the irradiation of spherical targets by laser beams might be expected to result in complete uniformity of irradiance. Here we restate the result that absolute uniformity on a spherical target is not attainable, even in principle.

G. Birkhoff[1] has shown that there exists only one spherically symmetric source-free solution of Einstein's field equations (Schwarzschild solution) which is static (i.e., field variables are independent of time). This is known as Birkhoff's theorem. Birkhoff's theorem has since been generalized[2] and, when applied to electromagnetic radiation, states that electromagnetic radiation cannot be truly spherically symmetric. This can also be shown in a more familiar way (e.g., see Jackson[3,4]).

First, consider a segment of a "spherical wave" focused at the target center with a finite coherence time τ_c equal to the pulse-width. It can be shown[5] that the normalized autocorrelation (or

Figure 7

Geometry illustrating the angle ϕ between the rays from two lenses, each of half-angle θ. The beam axes form an angle b with respect to each other. The optical axis of each beam is assumed to pass through the target center. The angle δ selects any ray between $\delta = \theta$ (on-axis ray) to $\delta = 0$ (marginal ray) for each ray pair considered.
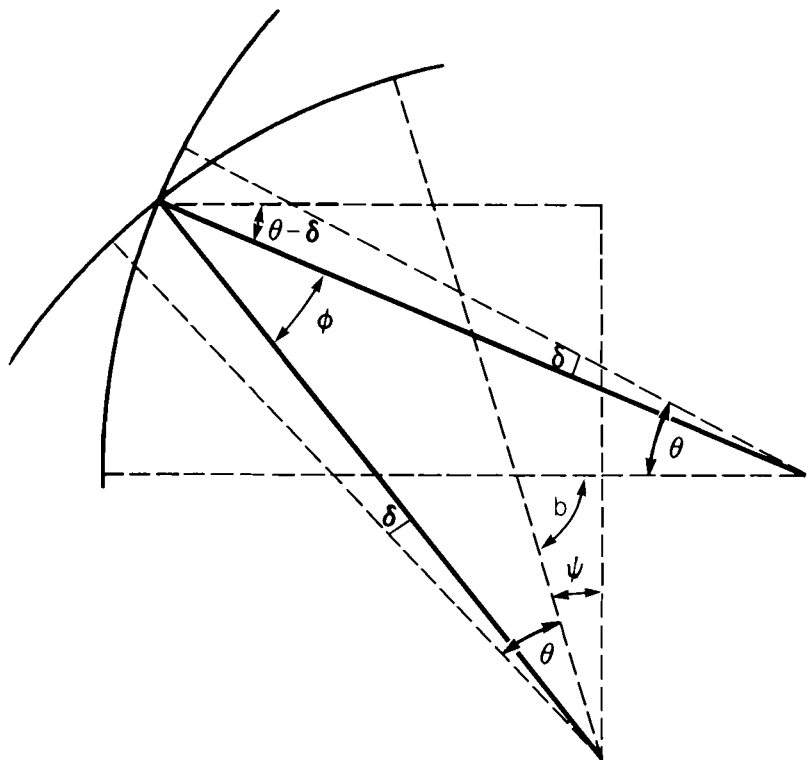
mutual coherence) function $\gamma(\vec{r_1}, \vec{r_2}, \tau)$ changes very slowly over any part of the target surface. Moreover, the cosine phase term will change rapidly because of the presence of the phase difference which is inversely proportional to the wavelength[5]. Thus over a portion of the target surface (such as the region covered by one beam), the average intensity will have negligible nonuniformity. In other words, the interference effect due to finite temporal coherence for a "spherical wave" on a spherical target approaches zero. Thus, we are justified in assuming perfect temporal coherence as far as illumination uniformity is concerned.

When a spherical target is irradiated by n monochromatic beams, the interference fringes in the overlapping region of the beams have the following characteristics:

1. The angle between two rays (or wavefronts) from any two beams is quite large. This can be seen from Figure 7. b and ϕ are angles between two beam axes and two rays respectively, and Θ is the lens half-angle. From Figure 7, it is clear that $b + \Psi = \phi + 2(\Theta - \delta) + \Psi$ or $\phi = b - 2(\Theta - \delta)$. Thus, $\phi_{min} = b - 2\Theta$. For the ZETA system, $b = 90°$, $\Theta = 22.5$, and $\phi_{min} = 45°$. With such a large angle, the spacing between fringes is given by $d = \lambda/\sin 45° = 1.4\lambda$, which is of the order of one wavelength.

2. The contrast between "bright" and "dark" interference fringes between any two beams is quite small for the six-beam ZETA system and not very large for the 24-beam OMEGA system due to the fact that the angle between two wavefronts is about 45° for ZETA and 28° for OMEGA. The contrast for multi-beam interference fringes will be even smaller.

3. Lens aberrations will further suppress the importance of interference fringes due to multiple beams[6].

Consequently, the interference fringes in the overlapping region are negligible.

Initially, the focused electromagnetic field in spherical geometry was treated in terms of Debye potentials[7]. The treatment of electromagnetic waves in a dense spherically symmetric plasma enables the matching of boundary conditions of tangential and normal components of $\vec{E}$ and $\vec{B}$. The treatment is very similar to Erkkila's dissertation[8] except that ponderomotive force effects and filamentation are also considered in addition to inverse bremsstrahlung and resonance absorption processes.

However, if diffraction is to be considered, then rigorous diffraction theory has to be applied, which is a major unsolved problem in itself. Fortunately, it has been established[9,10] that even in a large aperture spherical system [typically the angular semi-aperture (lens half-angle) can be up to 40°] scalar diffraction theory is still valid for describing the image field. Because the

ZETA and OMEGA systems use lenses of f/1.2 and f/3, with lens half-angles of 22.5° and 9° respectively, scalar diffraction theory is sufficient for our discussion of target irradiance for both systems.

Before proceeding with a detailed description of our latest results, a short summary of previous preliminary calculations performed (1976 to 1978) on the uniformity of illumination achievable on spherical targets for both the ZETA and OMEGA systems will be presented. This earlier work considered geometric optics with several intensity profiles and artificial absorption coefficient models which we shall discuss shortly.

The uniformity of illumination on a spherical target depends on the disposition of the beams, whole angle (or f/#) of the lens, focal position of the lenses, radial intensity profiles of the beam, absorption coefficients of the target, and any target misalignment error.

Leppelmeier[11] and Howard[13] have shown the necessity of using fast lens in order to obtain uniformity of illumination on a spherical target. This work[11,13] included the effects of different numbers of beams and their disposition. The number of beams,
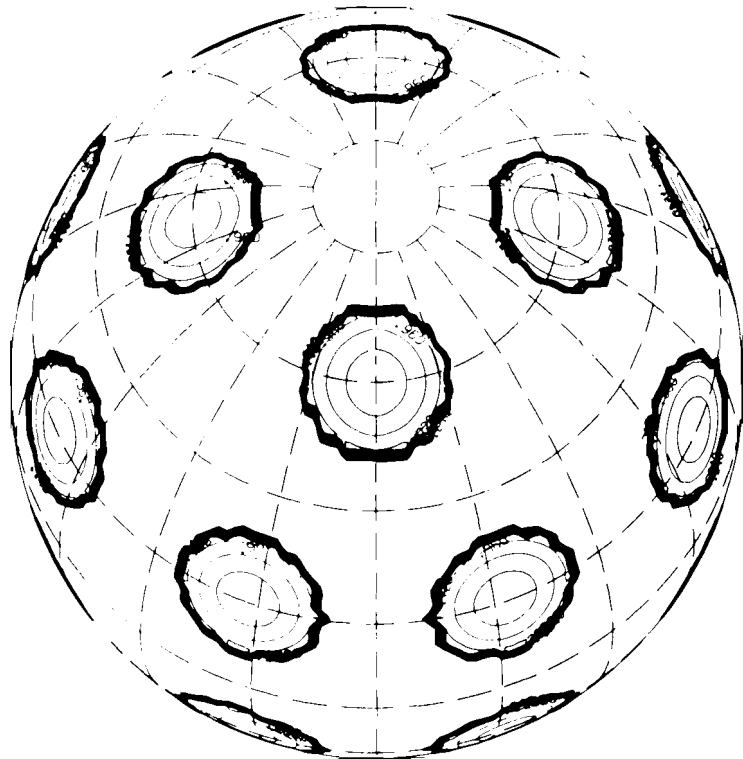

Figure 8

On target intensity contour plot from the OMEGA system for a reverse quadratic intensity profile (ratio = 0.2, focus = 0.2).

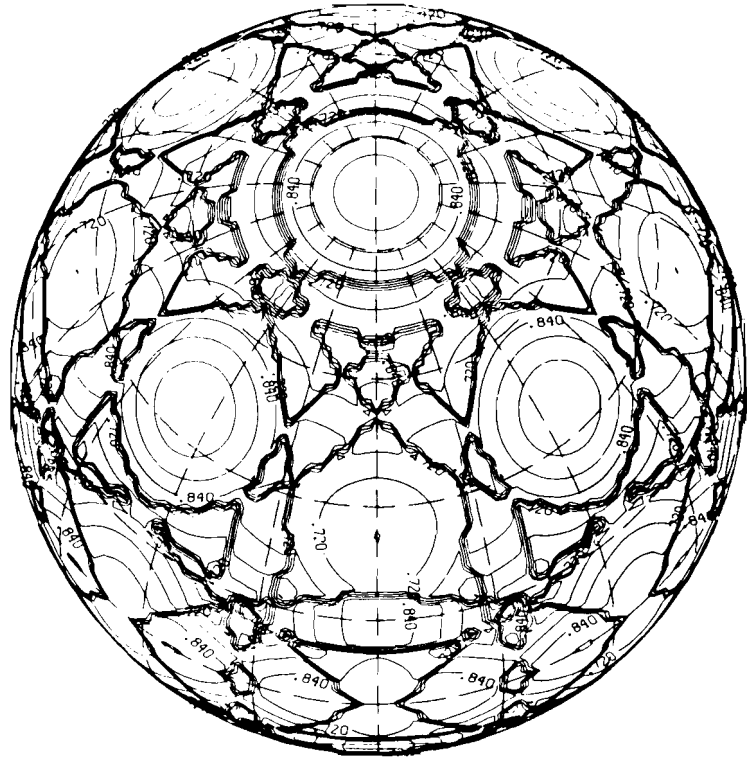Contour from 0.0 to 0.96 (Contour Interval of 0.06)

Figure 9

On target intensity contour plot from the OMEGA system for a reverse quadratic intensity profile (ratio =0.2, focus = 3.6).

Contour from 0.48 to 0.99 (Contour Interval of 0.03)

their geometrical arrangement, and the f/# of the lenses for both ZETA and OMEGA were decided based upon Leppelmeier's work; the work by Lee[12] was to determine how the uniformity of illumination depends on the remaining parameters.

In the preliminary simulations, different beam radial intensity profiles were considered:

1. Flat top $I(r) = I_o$,
2. Quadratic $I(r) = I_o[1-(r/R)^2]$,
3. Soft-supergaussian $I(r) = I_o \exp [-a(r/R)^5]$,
4. Reversed quadratic $I(r) = I_o [1-ratio (1-(r/R)^2)]$ with different depth to height ratios from 0.1 to 0.5.

Although many of the relevant absorption processes are qualitatively understood, the quantitative distribution of each process is not known. Thus in these studies different mixes of the various absorption coefficients appropriate to different absorption mechanisms have been considered. Results for a few mixed "legislated" absorption coefficients, which represent an approximation of experimentally observed values for the various processes, will be presented below. Nonuniformity in terms of the percentage of $\sigma/\bar{I}$ is plotted against the focal position in terms of target radii behind the target center for each absorption coefficient, where σ is the RMS deviation of the intensity and $\bar{I}$ is the mean intensity. An acceptable level of nonuniformity of target illumination ($\sigma/\bar{I}$) is assumed to be less than 10%.
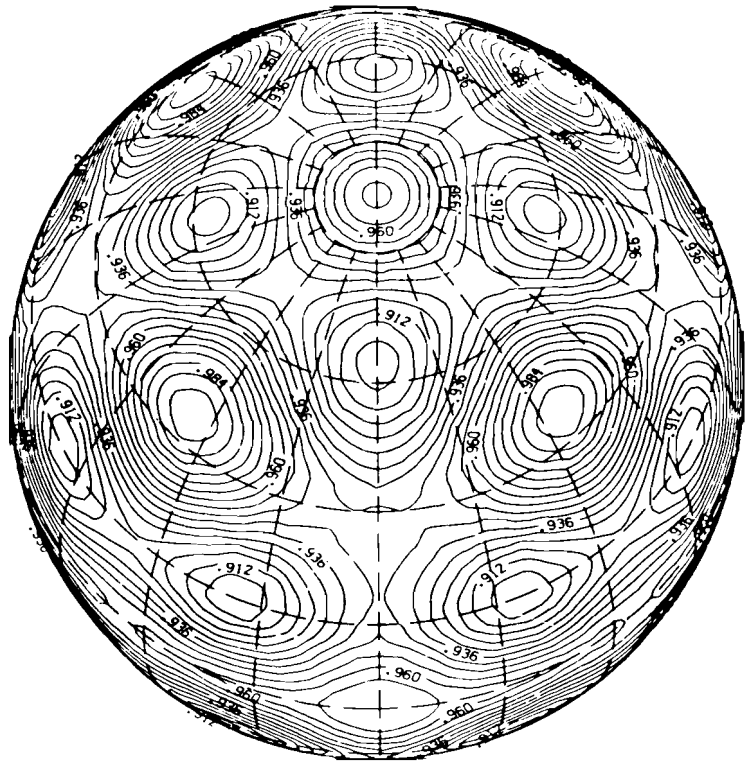
Figure 10

On target intensity contour plot from the OMEGA system for a reverse quadratic intensity profile (ratio = 0.2, focus = 5.6).

Contour from 0.894 to 0.996 (Contour Interval of 0.006)

Recently, longer pulsewidth and longer plasma scale lengths, together with conditions appropriate for $3\omega_0$ ("blue") irradiation experiments, have been considered. Contour plots of the intensity distribution on target, as well as plots of intensity at constant latitude Θ and longitude ϕ have been implemented. Figures 8 through 10 display contours of the intensity distribution on a target
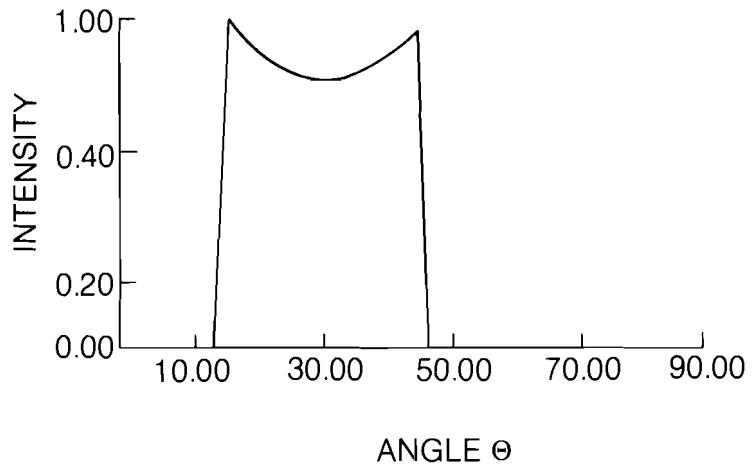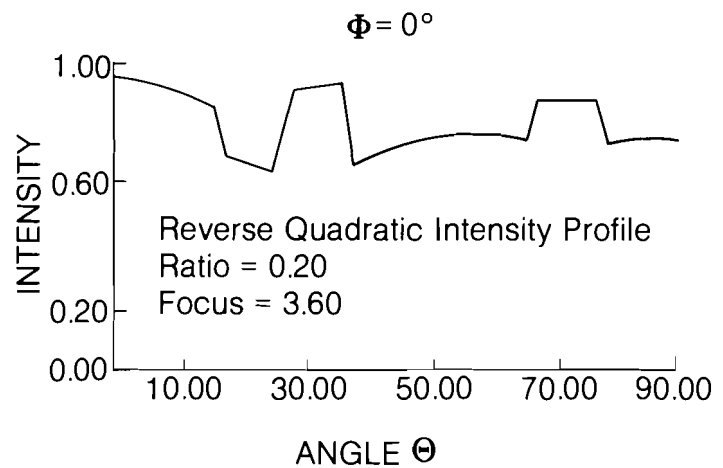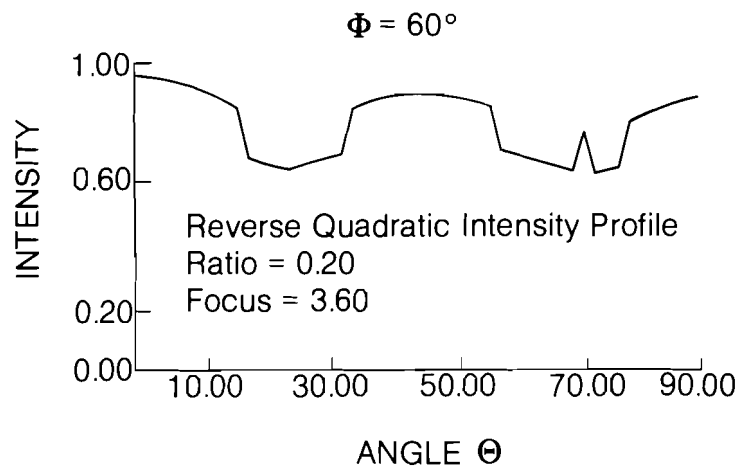

Figure 11

Intensity plot at constant longitude.

Φ = 0°

Figure 12
Intensity plot at constant longitude.

irradiated with beams having a reverse quadratic intensity radial profile (with depth to height ratio of 0.2).The focal position of each beam was varied for values 0.2,3.6,and 5.6 target radii behind the target center for the OMEGA system. For the three cases shown, the established plasma scale length was of the order of 40 μm, with an assumed total laser energy absorption of 45% (30% collisional absorption and 15% resonance absorption). An alternative representation of the intensity distribution on target is obtained by passing a plane through the intensity distribution at a constant latitude Θ or longitude ϕ. Figure 11 is the $\phi = 0$ plot for beams focused 0.2 target radii behind the target center. Figures 12 and 13 are the corresponding $\phi = 0°$ and $\phi = 60°$ plots. Figures 14 and 15 show the $\Theta = 40°$ and $\Theta = 85°$ plots for beams focused 3.6 target radii behind target center. Similarly, Figures 16 through 19 are plots for beams focused 5.6 target radii behind target center. In order to model the effects of both "short" and "long" pulses proposed for experiments, the absorption coefficients for the processes we shall present here are for

Φ = 60°

Figure 13
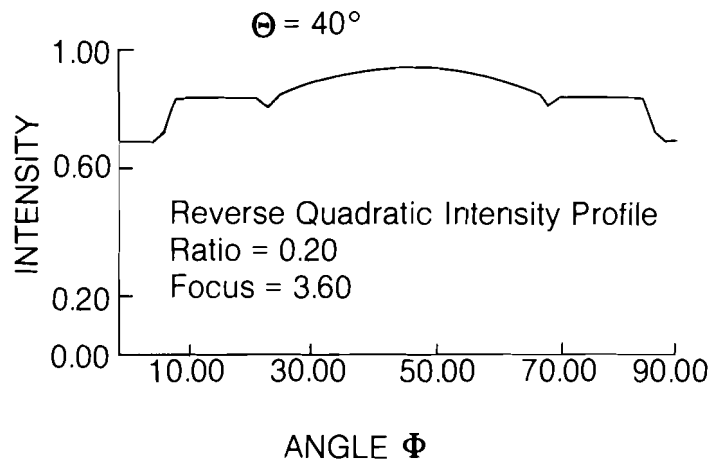*Intensity plot at constant longitude.*

Figure 14
Intensity profile at constant latitude.

both "short" and "long" plasma layers (these layers are characterized by plasma scale lengths of 3 and $20\mu m$ respectively) with:

1. A maximum amount of resonance absorption (up to 50% of the total absorption), and
2. A moderate amount of resonance absorption (up to 30% of the total absorption). The absorption coefficient is of the form: $A=aA_u + bA_b + cA_r$ where, a, b, and c are weight factors (constants). A_u includes all the absorption processes which are angularly independent (or weakly angularly dependent), such as ion acoustic turbulence[15,16]; A_b denotes the collisional processes proportional to $cos^5\Theta$ (inverse bremsstrahlung absorption for a ramp plasma profile)[17]; A. represents the resonance absorption process where the functional fit of Forslund et al.[18] has been used ($A_r = \xi$ $exp(1-2\xi)$ where $\xi=(2\pi L/\lambda)^{2/3}sin^2\Theta_0$ where Θ_0 is the angle of incidence, L the plasma scale length, and λ the wavelength of the incident radiation).
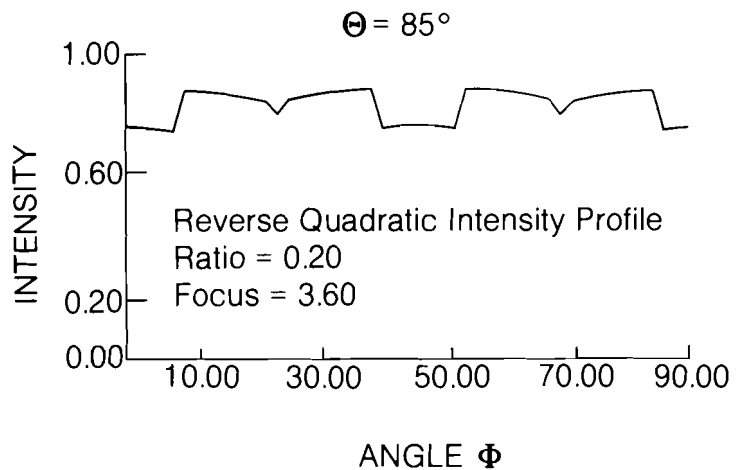

Figure 15
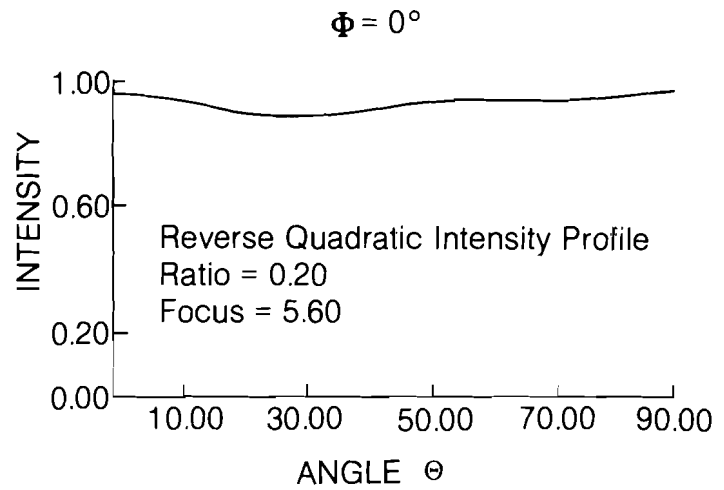*Intensity profile at constant latitude.*

$\Phi = 0°$

Figure 16
Intensity plot at constant longitude.

It should be pointed out that $\sigma/\bar{I}$ versus focal position curves for experimentally observed absorption processes are expected to lie in the region bounded by these two limiting curves at or near the focal positions studied. Nevertheless, these limiting curves are slightly optimistic in nature due to the fact that neither diffraction nor nonlinear effects, such as self-focusing or filamentation, have been taken into consideration in the model.

For supergaussian and quadratic intensity profiles, the $\sigma/\bar{I}$ versus focal position curves (for both models employing thick and thin plasma layers and assuming maximum resonance absorption) are seen to level off and approach 10% when the beams are focused more than 2.6 target radii behind the target center. Furthermore, the uniformity is seen to be quite sensitive to
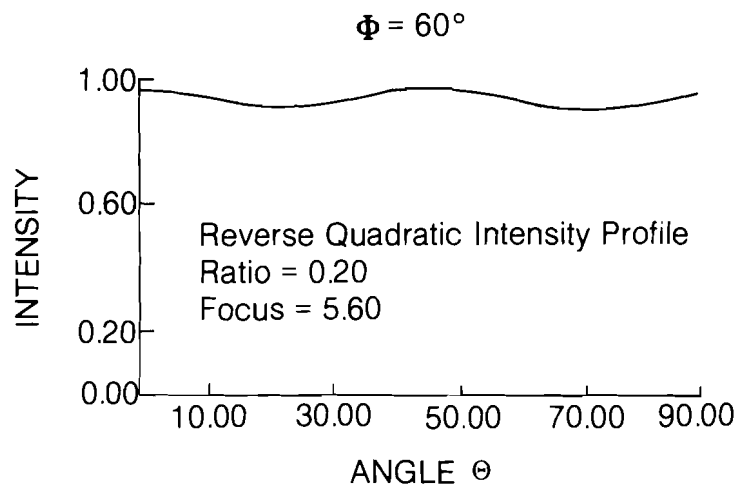
$\Phi = 60°$

Figure 17
Intensity plot at constant longitude.

$\Theta = 40°$

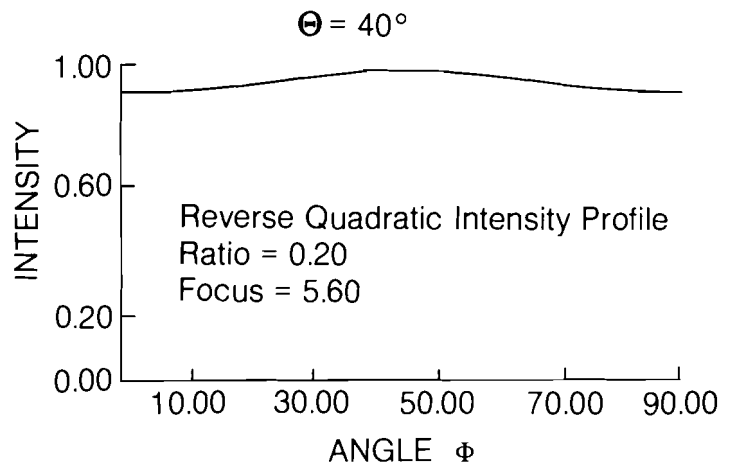Reverse Quadratic Intensity Profile
Ratio = 0.20
Focus = 5.60

Figure 18
Intensity profile at constant latitude.

target misalignment. Thus, from the standpoint of uniformity, both quadratic and supergaussian intensity profiles are not very suitable for target illumination for the ZETA subsystem of OMEGA.

For the flat top and reverse quadratic intensity profiles, the $\sigma/\bar{I}$ versus focal position curves for all absorption coefficients and all simulated intensity profiles are seen to have a relative minimum below 10% for different focal positions (Figure 20). Moreover, the curves for each absorption coefficient have the same qualitative features for different intensity profiles in this category. We have also found that even for different mixtures of various absorption processes, the curves lie close to one another. These results hold for both "long" and "short" plasma layers. Furthermore, the uniformity is less sensitive to misalignment errors compared to
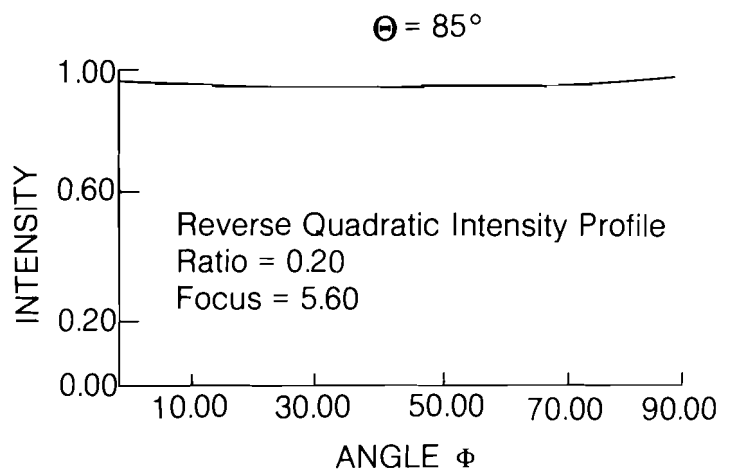
$\Theta = 85°$

Reverse Quadratic Intensity Profile
Ratio = 0.20
Focus = 5.60

Figure 19
Intensity profile at constant latitude.

that seen for the supergaussian or quadratic radial beam profile models. Nonuniformity ($\sigma/\bar{I}$) remains below 10% for target displacements from the chamber center for target position errors as large as 0.25 target radii.

The best focal position for each beam depends on the absorption processes taking place. Our simulations show that independent of the details of our model absorption processes and beam radial intensity profiles studied, the beam should be focused at or beyond 2.1 target radii behind the target center.

Recent experimental results with the ZETA system have verified these theoretical results and exhibit the same qualitative behavior[19] as our model curves. For the focal position at a distance b less than one target radius R behind the target center, considerable absorption nonuniformity has been observed. The experiments show that a steady improvement in uniformity is observed as b increases up to 2.7R, where the uniformity is quite satisfactory.
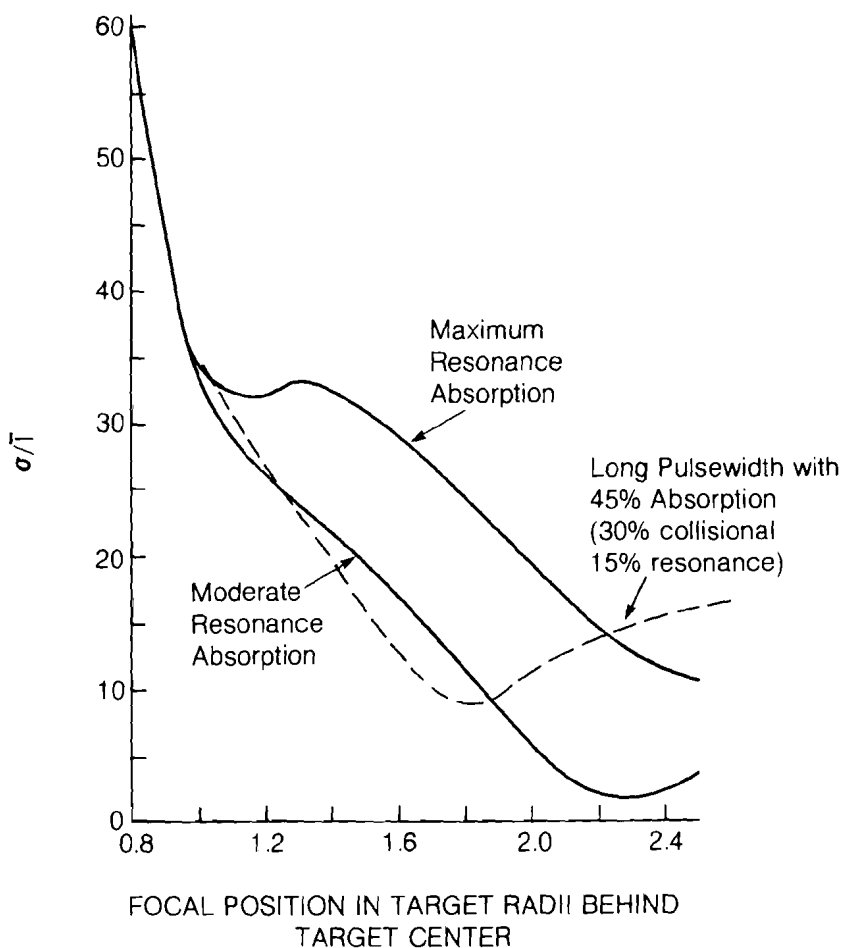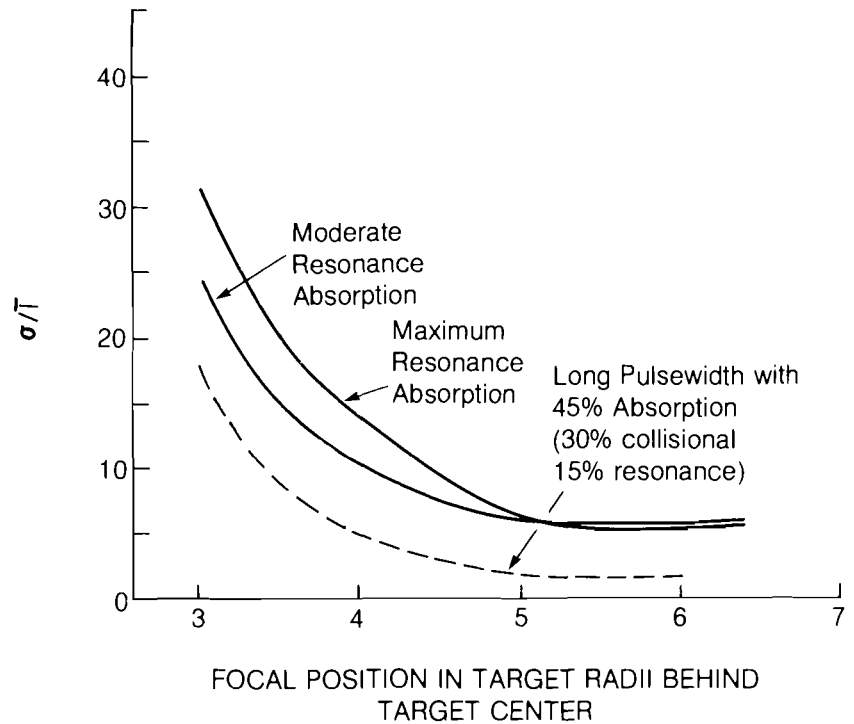
Figure 20

$\sigma/\bar{I}$ versus focal position ZETA with reverse quadratic intensity profile (depth to height ratio of 0.2).

FOCAL POSITION IN TARGET RADII BEHIND
TARGET CENTER

Figure 21

$\sigma/\bar{I}$ versus focal position for OMEGA with reverse quadratic intensity profile (depth to height ratio of 0.2).

Uniformity of illumination is expected to improve for the full OMEGA laser system over that of the ZETA subsystem due to an increase in the number of symmetrically arranged laser beams. Our numerical simulations of target illumination for the OMEGA system have confirmed that this is indeed the case. The curves for both "long" and "short" plasma scalelengths are clustered together. Furthermore, independent of the assumed beam radial intensity profiles, the curves asymptotically approach the 6% line (Figure 21). We conclude that if the beams are focused at or beyond 5.4 target radii behind the target center, nonuniformity of the illumination of 6% or less will be achieved on target. Moreover, the uniformity of illumination was found to be quite insensitive to reasonable target centering errors.

Alternate designs with different lens f/# for both the ZETA and OMEGA systems have been considered. The qualitative features of $\sigma/\bar{I}$ versus focal position curves are similar to the original designs, differing only in the optimal focal position and the minimum value of $\sigma/\bar{I}$.

In summary, a nonuniformity ($\sigma/\bar{I}$) of 10% or less can be achieved for the ZETA system, provided the radial beam intensity profiles are neither like the supergaussian nor quadratic profiles, and 6% or less nonuniformity can be attained for the OMEGA system. Long pulsewidth simulations, corresponding to an established plasma scalelength on the order of 40 μm have

17

recently been considered for both the ZETA and OMEGA systems. The total laser energy absorption for the long pulsewidth case is assumed to be 45% (partitioned as 30% collisional absorption and 15% resonance absorption). These simulation results show that the use of long pulsewidth laser pulses on the ZETA system results in nonuniformity of illumination similar to those obtained in the short pulse research. However, simulations of long pulse-width pulses on the full OMEGA system result in nonuniformity of illumination of order less than 3% for the model beam profiles considered.

At present, the following improvements to our computer simu-lation of illumination uniformity are being considered:
1. to include scalar diffraction effects,
2. to model absorption coefficients in a more self-consistent way,
3. to calculate uniformity effects using measured beam radial intensity profiles in contrast with the model profiles we have described here, and
4. to model the effects of system energy imbalance.

Section 2
PROGRESS IN LASER FUSION

2.A Observation of Brillouin Sidescatter in Laser-Produced Plasma

We have recently obtained spectrally resolved measurements of scattered light from spherical targets at angles between 26° and 56° with respect to the laser axis. These experiments were designed to help distinguish between stimulated Brillouin scattering and reflection of refraction from the subcritical region. From these measurements we conclude that the sidescatter observed is attributable in most cases to Brillouin scattering.

Both theory and experiment have shown that appreciable Brillouin scattering will only occur for plasmas with long scalelengths. These long scalelengths are very likely to be important in future laser fusion experiments particularly those presently under consideration for UV, "blue," light. In order to produce these long scalelengths, we have used two different type pulses:
1. a 140 psec (FWHM) pulse following an intentional pre-pulse[20],
2. a 700 psec (FWHM) pulse, temporally Gaussian with no prepulse.

This experiment used one beam of the Glass Development Laser (GDL) at the Laboratory for Laser Energetics[21]. The 80 to 90 μm diameter glass microballoon targets were irradiated by circularly polarized laser light ($\lambda = 1.054\mu$m) at powers of up to 100 GW with pulse lengths of (A) 140 psec and (B) 700 psec. For
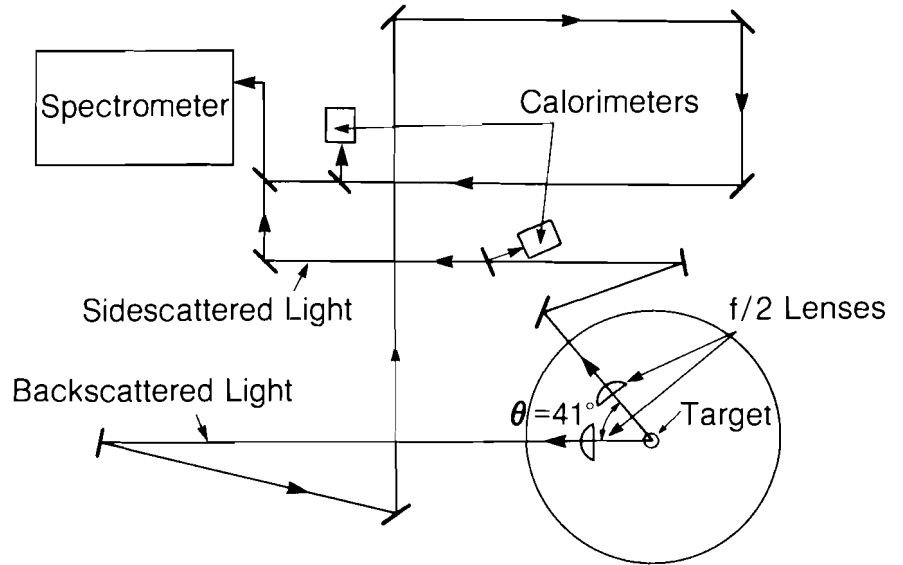
Figure 22
Experimental layout for sidescattering at $\lambda_L = 1.06\mu m$.

most of the type (A) pulses, a prepulse with controlled magnitude and timing was inserted ahead of a main pulse to simulate an extensive underdense plasma region which would result from the use of a longer pulse. The prepulse energy was typically 1% of the main pulse energy, and the time between pulses was 1 nsec. An f/2 aspherical lens was used to focus the incident beam onto the target. The focal spot size was determined from x-ray pinhole photographs to be approximately 35 μm in diameter. The peak intensity was between 10^{15} and 10^{16} W/cm^2 in both cases. Figure 22 shows the experimental setup. The light which was directly backscattered through the focusing lens was reduced in size, collimated via an inverse telescope, and split into two beams for energy and spectral measurements. The sidescattered light was collected by an identical f/2 aspherical lens placed at 41° to the incident beam axis. This sidescatter beam was also analyzed for both energy and spectrum.

A 1 m Czerny-Turner grating spectrometer with 1 Å resolution was used for both back and sidescattered light spectra which were recorded on Kodak 4143 highspeed IR film.

An example of both back and sidescattered light spectra obtained with two different pulse shapes is shown in Figure 23. Figure 23a, which illustrates a type (A) pulse at laser intensity of 5 x 10^{15} W/cm^2 showed a red shift of the peak of ~3 Å for the backscatter and ~5 Å for the sidescatter from the ω_L incident laser frequency and a maximum shift 50 Å and 40 Å respectively. In separate experiments but with the same type (A) pulse, the hot electron temperature T_{HOT} and the typical density scalelength were measured to be 10 KeV[22] and 20 μm[23] respectively. The

Brillouin scattering threshold for an inhomogeneous plasma is given by[24]:

$$P_{SBS} > (1.6 \times 10^{14})\, T_e \text{ W/cm}^2,$$

where T_e (KeV) is the electron temperature driving an ion acoustic wave in an underdense plasma. Thus, since T_{HOT} is the upper limit for T_e, our laser intensity was well above the threshold, and the measured spectral red shifts were considered due to the stimulated Brillouin process. In the type (A) pulse we see no evidence for an unshifted (ω_L) spectral component in either the back or sidescattered light. The type (B) case of the 700 psec pulse at the intensity of 3.4×10^{15} W/cm² showed a somewhat different pattern. In addition to the red-shifted spectrum seen in both back and sidescattered light, the sidescattered spectrum contained a significant unshifted component in Figure 23b. This unshifted component is assumed to come from refracted incident light. Specular reflection may be ruled out as there is no comparable component in the direct backscatter. This clearly indicates the ability of this experiment to differentiate between the stimulated scattered component and the refracted or reflected light through angular resolved spectra. The finer angular distribution of the scattered light was measured using portions of the sidescatter collection lens. A mask with three apertures was used to give equal solid angle observations horizontally at $\Theta = 31°, 41°,$ and $51°$ with respect to the incident laser beam axis. The effective f number for each aperture was 6.7.
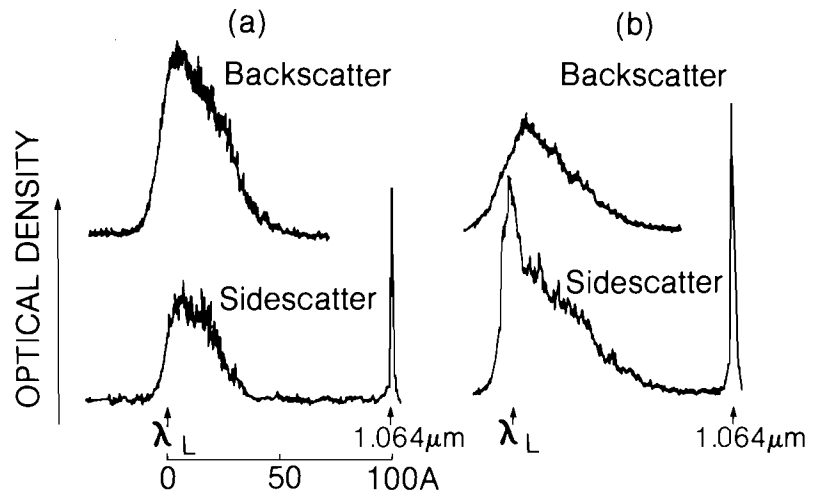

Figure 23

Back and sidescatter spectra for
a. type (A) pulse (prepulse + 140 psec pulse)
$I_L = 5 \times 10^{15}$ W/cm²
b. type (B) pulse (700 psec pulse)
$I_L = 3.4 \times 10^{15}$ W/cm²
OD is not in scale.

The measured angular energy distributions for two power levels are shown in Figure 24. In both experimental curves, the scattered light intensity falls rather rapidly as the angle increases. The decrease in intensity with scattering angle is somewhat more rapid than would be predicted by a one-dimensional model[25]. This result is not surprising since the plasma expansion geometry produced by illuminating 35 μm of a
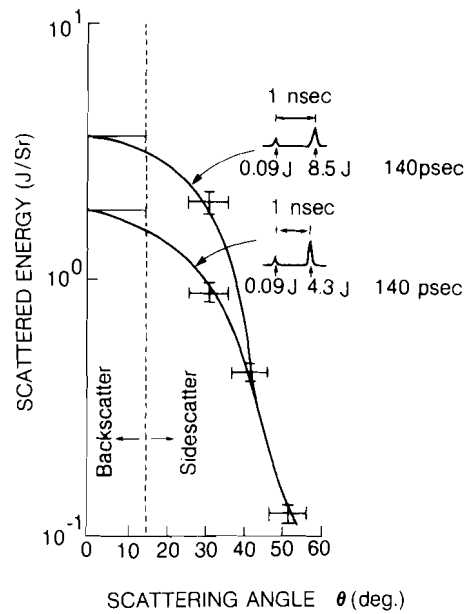
Figure 24

Angular distribution of stimulated Brillouin scatter for type (A) pulse. θ: angle with respect to incident laser axis.

80 μm diameter microballoon is unlikely to be represented by a one-dimensional planar expansion. The use of circular polarization for the incident beam allows one to assume axial symmetry for the scattered light. With this assumption of symmetry, the solid angle of the measured sidescatter light (S_1, $26° \leq \Theta \leq 56°$) was about 10 times larger than that of the backscattered light through the focusing lens (S_{FL}, $0° \leq \Theta \leq 15°$) as seen in Figure 25. Thus, although the energy scattered per unit solid angle (J/Sr) falls rather sharply with increasing angle (see Figure 24), the effective solid angle was large enough that the integrated energy in sidescattering was significant compared to
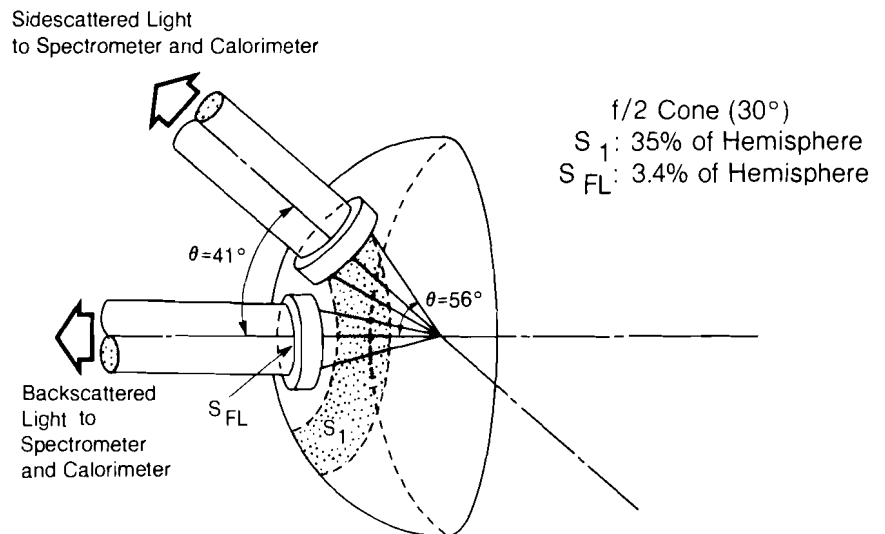

Figure 25

Sidescatter measurement configuration.

the backscattered value. Table 2 summarizes the scattered energies for both back and sidescattering. The total sidescatter energy was calculated by interpolating the angular distribution from $\Theta = 15°$ to $\Theta = 26°$. For the high intensity prepulsed case (A), we find that the total sidescatter energy is approximately 55 percent of the incident compared to 12 percent in the direct backscatter. Above 2 to 3×10^{15} W/cm², the Brillouin scattering appears to saturate at the above values [26,27,28].

In summary, these measurements show that for laser plasmas with appreciable density scalelengths, most of the scattered light (out to angles of 60° to the incident beam) can be attributed to the stimulated Brillouin process. Assuming axial symmetry, the energy measurements show that the Brillouin sidescatter can represent more than 50 percent of the incident light.

Table 2

Fraction of scattered energy (%) compared to the incident energy at two different intensities for type (A) pulse. Prepulse energy was kept constant for each intensity.

| Laser Intensity	Brillouin Backscatter	Brillouin Sidescatter
3×10^{15} W/cm²	12 %	52 %
7×10^{15} W/cm²	12 %	55 %

2.B Progress in Radiationally Cooled Target Experiments

Over the last few months we have extended and refined the measurements of radiationally cooled, Argon filled target implosions. As summarized in the discussion of radiationally cooled targets in Volume 1 of the LLE Review, such implosions lead to highly compressed densities, and the x-ray line spectrum of the Ar^{+16} and Ar^{+17} ions enables a direct determination of core densities and temperatures near the time of peak compression in the implosion event. Densities as high as 6 g/cm³ and temperatures of about 1 KeV have been measured in this way in our experiments.

The recent set of experiments added a variety of parametric effects to extend our previous results:
1. The effect of different beam focusing conditions on the core compression.
2. The compression of a fill mixture of Argon and thermonuclear fuel rather than just Argon.

Figure 26
Higher compressed density with better symmetry focusing.
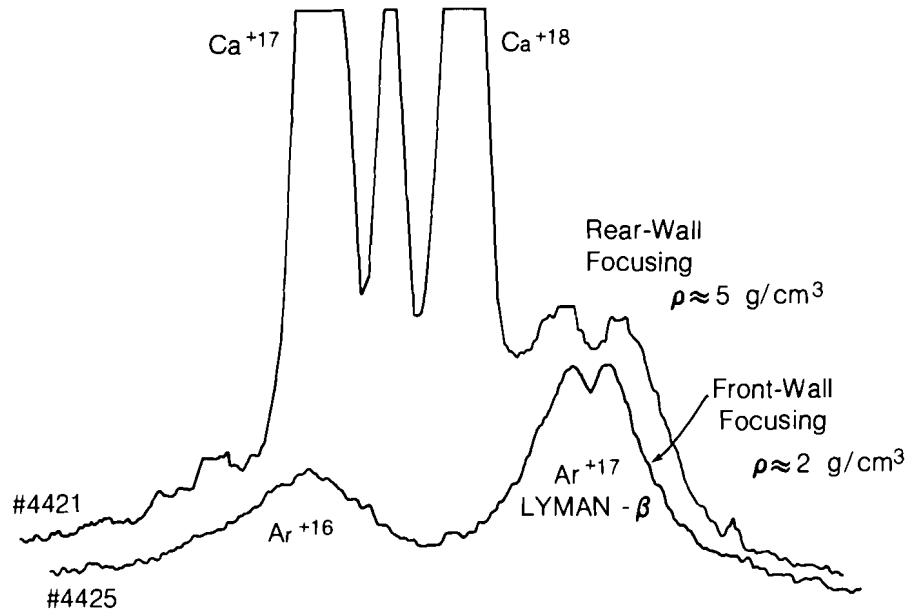
3. Time resolved x-ray measurements of radiationally cooled targets (where the radiation around peak compression decays very fast).
4. Imploding a target of low pressure Argon fill which leads to a high volumetric compression ratio (~1000).
5. Improved (lithographically produced) slits to image the target for each spectral line with a spatial resolution of 7 μm. Such information used with a computer code to perform the required deconvolution enables us to corroborate the determination of density by spectral profiles.

We illustrate below some of the recent results and briefly discuss their significance. The laser and target parameters for the four shots we discuss in these examples are summarized in Table 3. Figure 26 shows that focusing the laser beams on the rear surface of the target produces broader Argon line profiles, indicating a higher peak density, as compared with focusing on the front surface of the target. X-ray imaging (in two dimensions)

Table 3

Laser and target parameters for the shots used as examples in Figures 25 through 30. +2R focusing means two target radii behind center.

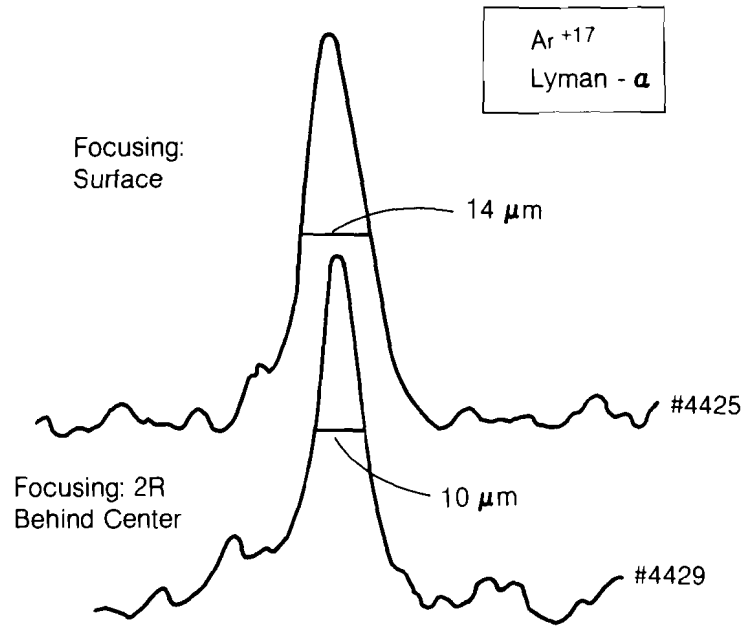| Shot Number	Absorbed Laser Energy (J)	Pulse Width (psec)	Focusing W/r to Center	Target Diameter (μm)	Wall Thickness (μm)	Plastic Coating (μm)	Ar Fill Pressure (atm)
4421	35	68	+1R	50	1.65	2.5	50
4425	47	87	-1R	46	1.40	2.8	50
4429	32	75	+2R	47	2.30	2.5	50
4436	35	65	+1R	47	1.86	3.5	3

Figure 27

Smaller compressed Argon core achieved with higher symmetry focus.

shows that better spherical symmetry is achieved in the former case. These results demonstrate that better symmetry leads to higher compression.

Figure 27 shows that focusing two target radii behind the target center (which, as judged by x-ray pinhole photographs, yields best symmetry of illumination) leads to a smaller compressed core as compared with focusing on the front surface of the target. The curves in Figure 27 pertain to a single Ar^{+17} line (the $2 \rightarrow 1$ transition at 3.321 KeV) as a function of a spatial (lateral) coordinate.

Figure 28 compares the spectrum in the range of 3-4 KeV for two focusing conditions: (a) two radii being the center, and (b) rear surface. One striking difference between the two is in the intensity ratios between the two Argon resonance lines at 3.140 keV and 3.321 keV and with the nearby dielectronic satellite lines marked S. The explanation of these differences is that the target in shot no. 4429 is compressed to a higher ρR. The higher ρR leads to a higher intensity of Argon lines which is clearly evident for the S lines. However, the resonance lines (of the Ar^{+16} and Ar^{+17} ions) do not increase because of saturation which is characteristic of heavily absorbed resonance lines. Another striking difference between the two spectra of Figure 28 is the severe attenuation of Ca^{+18} lines in going from the lower to the upper spectrum in the figure. This indicates a significantly lower temperature in shot no. 4429. It is characteristic of radiationally cooled targets that higher density is caused by (and in turn is causing) a lower temperature.
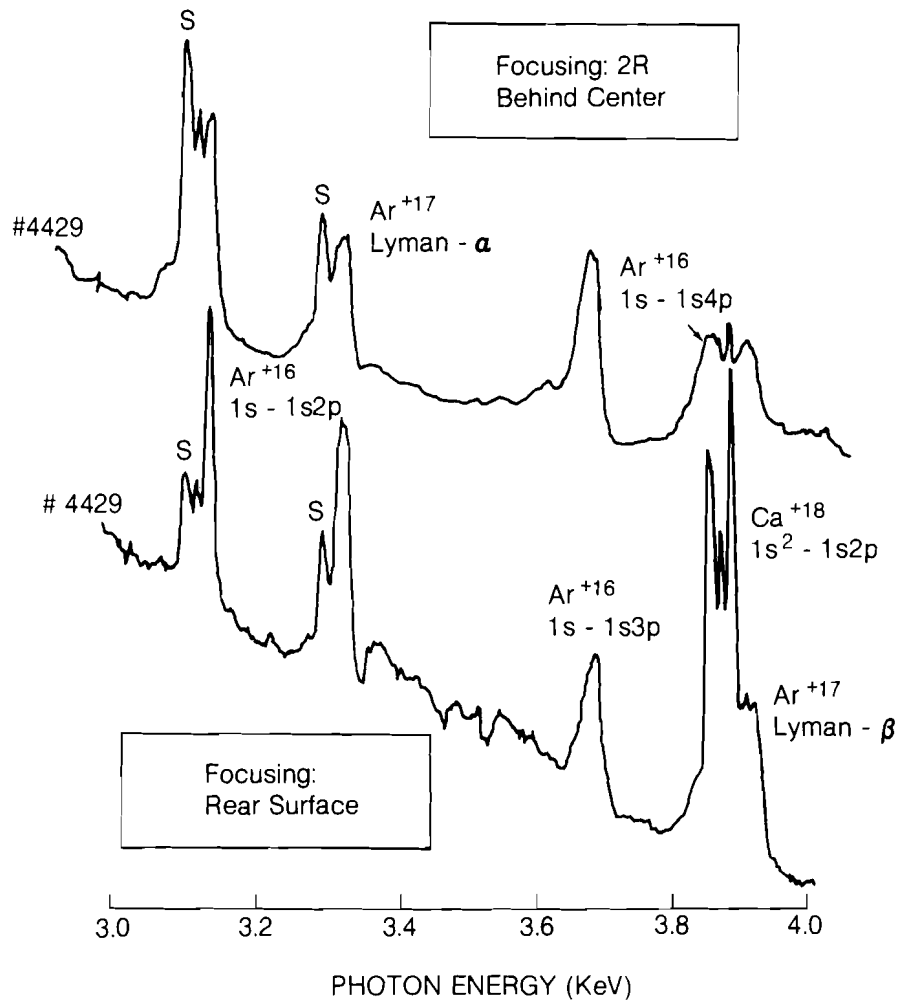
Figure 28
Higher ρR and increased radiation cooling in higher symmetry focusing.

Figures 29 and 30 show parts of the spectrum for a target of 3 atmosphere fill pressure of Argon (this fill is lower than most other target shots in this series). The Stark-broadened profile of the Ar^{+17} Lyman-β line (3→1) indicates a compressed core density of 5 g/cm³. If the whole Ar fill gas were compressed, this would indicate a volumetric compression ratio of 1020 which corresponds to a size of the compressed Argon region of 4.5 microns. To corroborate this, we show in Figure 31 a one-dimensional image of the target at the Lyman-β line radiation obtained with a resolving slit of width 6μm. The lower scan is taken at a spectral position off the Argon line, and it shows the continuum radiation which has to be subtracted from the upper curve to obtain the net radiation of Argon. In doing so, it is clear that we should get a small emission region whose image is limited by the slit resolution. The results thus provide an indication, but not a proof, of the validity of the high compression deduced from the spectral profile of Figure 30.
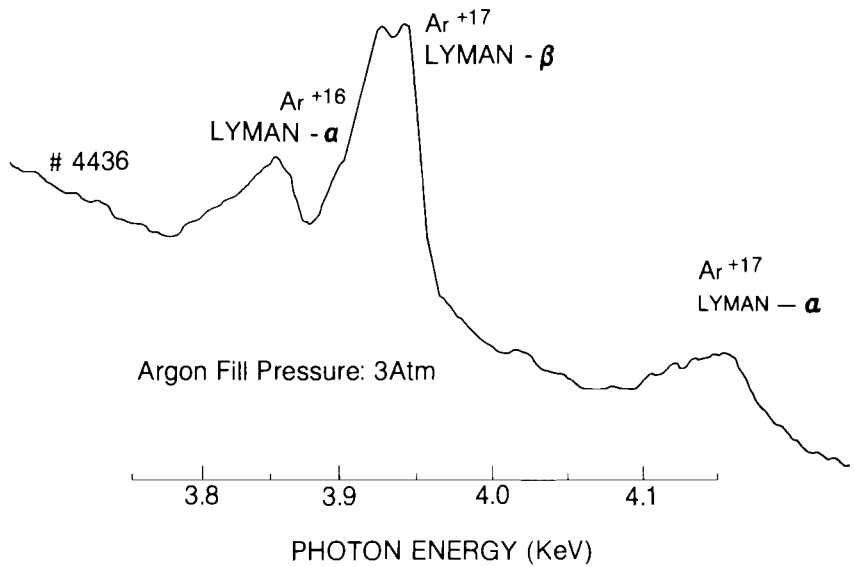
Figure 29

Asymmetry of Lyman-β Stark profile in low Argon fill pressure implosion.

Finally, an interesting feature in Figures 29 and 30 is the asymmetry of the Lyman-β profile: The higher energy peak is more intense than the lower energy peak. This is particularly evident when we consider that the underlying continuum rises for lower energies (see Figure 29). This asymmetry, not currently accounted for by the theory of Stark broadening, is thought to be caused by shielding of the nucleus from the radiating electron by neighboring electrons of the plasma. This effect, thought to exist in very high density plasmas is now under active study.
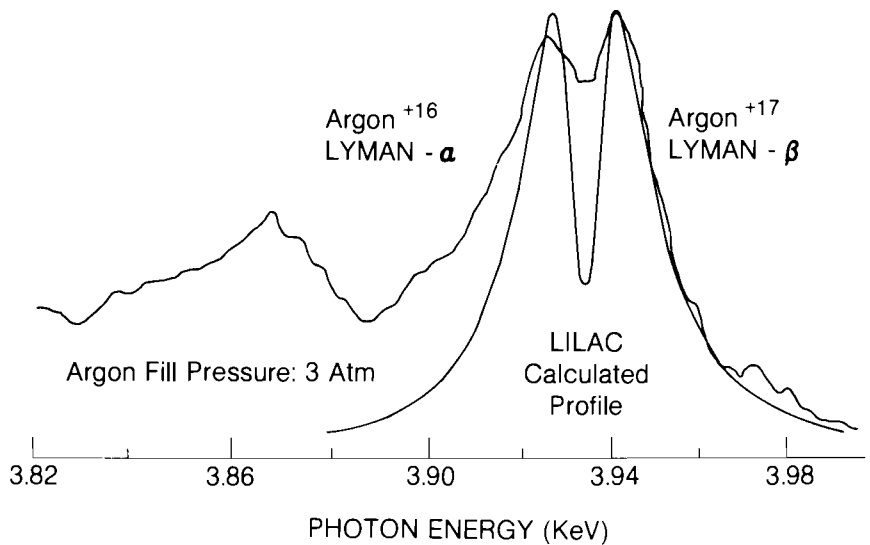
Figure 30

High density and asymmetric Lyman-β profile low Argon fill pressure implosion.
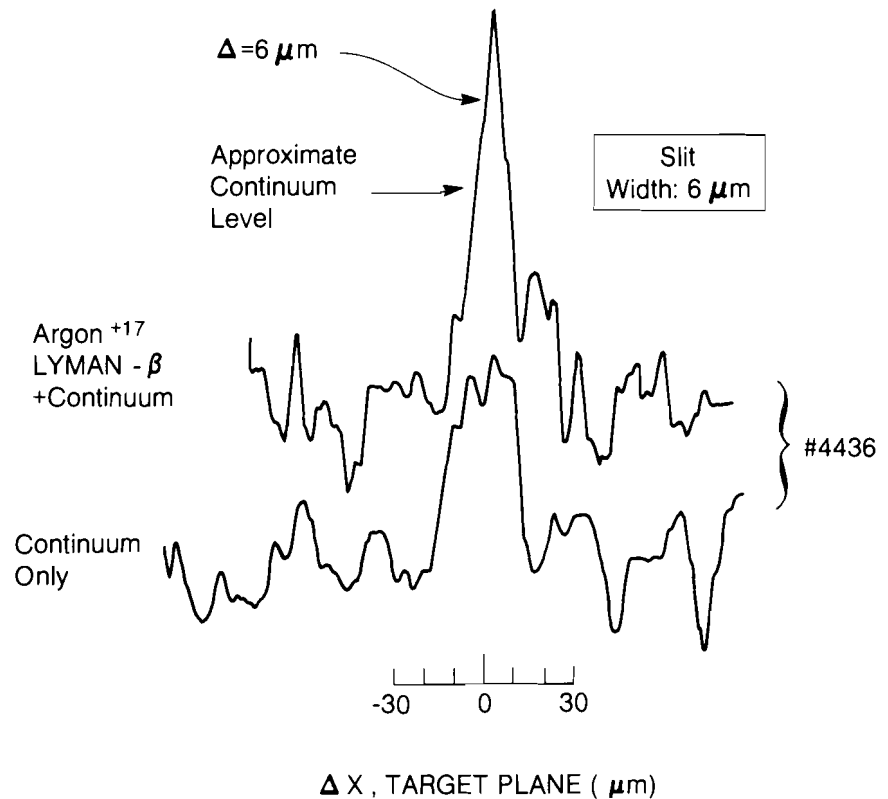
Δ=6 μm

Approximate Continuum Level

Slit Width: 6 μm

Argon +17 LYMAN - β +Continuum

Continuum Only

} #4436

-30   0   30

Δ X , TARGET PLANE (μm)

Figure 31
Small compressed Argon core achieved with low fill pressure (3 atm).

2.C   Calculations of the Wavelength Dependence of Absorption

One of the many advantages of using short wavelength radiation as a fusion driver is the increased collisional absorption expected. The laser radiation penetrates to higher densities where the plasma is more collisional and where collisional absorption (inverse bremsstrahlung) is more effective. In general, inverse bremsstrahlung is believed to be the dominant absorption mechanism at any wavelength at low laser irradiation intensities; as the intensity is increased, the plasma becomes hotter, and therefore less collisional, and the absorption decreases. (At still higher intensities the ponderomotive force of the laser steepens the density profile and resonant absorption becomes the dominant mechanism, but the absorption will then be only ~30%, independent of wavelength.) The intensity point at which the absorption falls off from values near 100% is believed to increase strongly as the laser wavelength decreases; therefore, by using short wavelength laser radiation, a high absorption may in principle be achieved at much higher intensities. Additionally, the fraction of energy coupled into suprathermal electrons is simultaneously reduced.

SAGE is a two-dimensional hydrocode which has been under development at LLE over the last few years. The code is Eulerian, and uses an orthogonal grid with arbitrary mesh spacings in each direction. It supports planar, cylindrical, and spherical geometries, and may be run in one or two dimensions. Details of the code may be found in Reference 29.

The only absorption process modeled fully in SAGE is inverse bremsstrahlung (IB). In all the calculations described here, the laser radiation is incident normally upon the target, and a straight line approximation is used to describe the ray paths. This is a reasonable assumption, since two-dimensional calculations show that the critical surface never moves very far out from the initial target surface, and remains approximately parallel to its initial location, even for long pulses when the flow far from critical becomes divergent. Generally, most absorption occurs very close to critical even for long pulses because of the strong density dependence of the inverse bremsstrahlung coefficient:

$$K_{IB} = K_c \frac{(n_e/n_c)^2}{\sqrt{1 - n_e/n_c}} . \qquad (1)$$

In order to accurately calculate the IB absorption, SAGE makes use of analytic formula for the integral of K_{IB} within each cell. This procedure ensures good convergence with respect to zoning. For example, if the true spatial profile $n_e(x)$ is exponential, SAGE will calculate the correct integral of K_{IB}, however coarse the zoning.

This picture may, however, not be so simple because it is generally accepted that for the intensities and laser pulse lengths of several nsec required for laser fusion, Brillouin instabilities in the underdense plasma may cause a substantial fraction of the incident laser energy to be reflected or scattered before it reaches the absorption region near the critical density. It is obviously imperative to understand how much energy can be coupled into the target under different circumstances for successful design of laser fusion targets. We have commenced by calculating the absorption for a wide variety of experimental conditions under the assumption of purely "classical" absorption physics, and we have obtained the surprising result that all of the fall-off of absorption at high intensities that has been observed in a wide range of recent experiments may be explained on the basis of this simple model, i.e. excluding such processes as Stimulated Brillouin Scattering (SBS). If our conclusion is correct, this is a significant and encouraging result.

In the sections below we describe the two-dimensional hydrocode SAGE, and calculations performed on SAGE to look at absorption and backscattering. For different irradiation geometries, laser pulsewidths and target materials, for four different laser wavelengths, and over several orders of magnitude of incident intensity, SAGE calculations are seen to be reasonably close to experimentally obtained results.

In addition, in the runs described below, SAGE dumps 15% of all energy reaching critical into a "non-thermal" electron distribution, as a Maxwellian described by a hot temperature T_H obtained from the local intensity according to the model of Reference 30. This purely ad hoc prescription provides a means of producing the supra-thermal electron component observed in many experiments and approximates the resonant absorption process which occurs at high intensities. When inverse bremsstrahlung is dominant, this additional energy source is insignificant because 15% of the energy reaching critical is a small quantity. When resonant absorption is dominant the 15% may be an underestimate, but this regime is not of great interest as the total absorption will then be small (<30%).

The key to an accurate calculation of IB absorption is the electron temperature T_e in the critical region, since

$$K_c \sim Z n_c T_e^{-3/2}. \quad (2)$$

As the temperature increases both K_c and the absorption, A, decrease, T_e is determined from the incident laser flux I by how effectively the absorbed energy is transported from the critical region to the ablation region, and may be estimated[31] by equating the absorbed energy flux (AI) to a multiple f of the "free-streaming limit":

$$AI = f (n_e k T_e) \sqrt{k T_e/m_e}. \quad (3)$$

SAGE, in common with other laser fusion hydrocodes, does not allow higher heat fluxes than that given on the right hand side of (3). The importance of the parameter f in modeling experimental data has been understood for some time[32].

A simple scaling law for IB is easily obtainable from Equations 2 and 3. For a plasma of scalelength L, the absorption A is a function of $K_c L$, where K_c is K_{IB} evaluated at critical ($n_c \propto \lambda^{-2}$) neglecting the square root term in Equation 1. Since

$$K_c L \sim Z n_c T_e^{-3/2} \times L \sim Z n_c (f n_c/I) \times L \sim ZfL/I\lambda^4,$$

we find that the absorption is a function of the quantity

$$Q = \frac{fZL}{I\lambda^4}. \quad (4)$$

For example, tripling the laser frequency allows the same absorption to be obtained at an intensity $3^4 = 81$ times greater, assuming that f, Z, and L remain unchanged.

Care must be exercised in applying Equation 4 because L is an unknown quantity which may depend on any of the other parameters in the formula as well as on other quantities such as the pulse length and target geometry. A hydrocode is required to
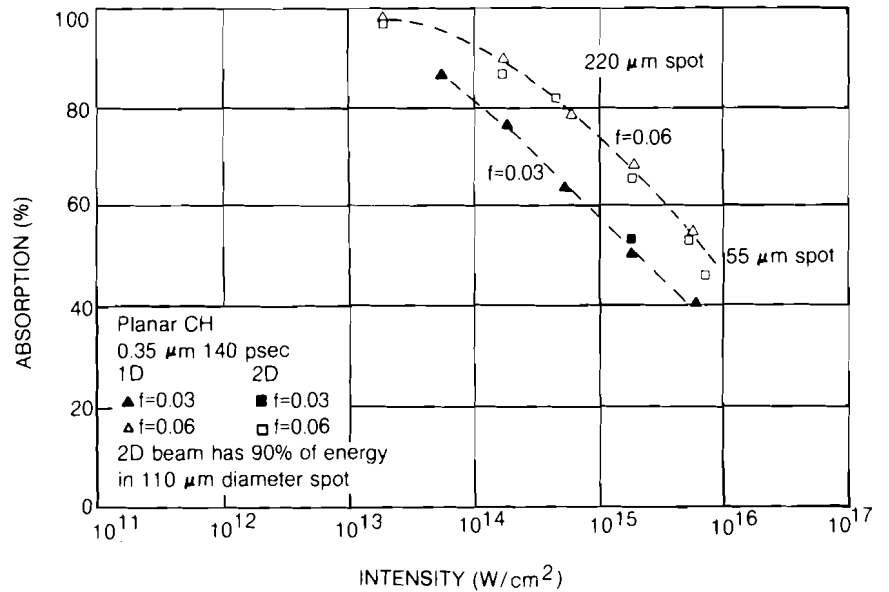
Figure 32

SAGE 1D and 2D calculations of A(I) for f=0.03 and 0.06, for 140 psec pulses of 0.35μm radiation on planar CH targets.

Nominal intensity of Gaussian 2D beam must be defined as the power divided by the area containing 90% of the energy.

accurately calculate L. (For example, L may decrease as f is decreased, as Z increases, or at high intensities where ponder-omotive steepening becomes important.) In addition, we are assuming that f is a basic physical quantity, independent of the other parameters, and this may not be correct although there is growing evidence that f varies very little.

SAGE also uses a tabular equation of state (SESAME[33]), which is important because it enables the code to treat spatially and temporally varying ionization states and the specific heat associated with ionization under the implicit assumption of local thermodynamic equilibrium. The LTE approximation is usually accepted to be valid over a wide range of laser intensities and pulse widths for low- to moderate-Z materials, such as plastics, glass, etc. The energy deposited into the non-thermal electron distribution is treated by a multi-group flux-limited diffusion model (using typically 20 groups). The radiation emitted from the plasma is calculated from the Los Alamos Astrophysical Library tables[34], and is transported by a similar multi-group diffusion model; typically 48 frequency groups are calculated.

Several physical effects are omitted from the calculations presented here. These include Stimulated Brillouin Scattering (SBS), magnetic field generation, non-LTE effects, ponderomotive steepening effects, and a high intensity inverse bremsstrahlung IB reduction factor[35].
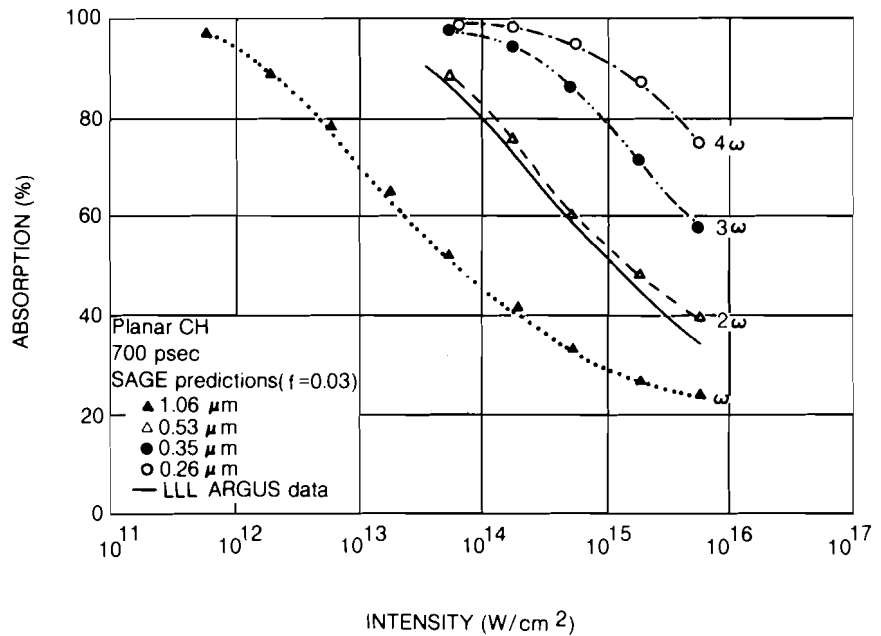
Figure 33

SAGE calculations of A(I) for f=0.03, for four different wavelengths, for 700 psec pulses and planar CH targets. The solid line is a fit to recent Livermore ARGUS data[36].

Predictions for the absorption A versus intensity I are shown in Figure 32 for 140 psec Gaussian pulses at $\lambda = 0.35\mu$m on planar CH. The two curves are for two values of the flux limit parameter (f = 0.03 and 0.06). Notice the sensitivity to f: for I = 10^{15} W/cm², the difference in A between the two cases is nearly 20%. The triangular points are for 1D planar calculations, and the square points are 2D calculations. The latter calculations use a spatially Gaussian radial beam profile whose nominal intensity is obtained by dividing the total power by the area containing 90% of the beam energy. (The normal intensity defined in this way provides a good estimate of the average intensity in the beam.) Two of the 2D calculations were performed using focal spots with respectively half and twice the radii of the other spots. The close correspondence between the 1D and 2D calculations suggests that to lowest order the absorption is not affected by 2D effects, allowing 1D planar runs to be used to map out the A(I) absorption characteristics.

Predictions for A(I) for the absorption on plastic at a few wavelengths of current interest are shown in Figure 33 for a 700 psec laser pulse and a flux-limit parameter f of 0.03. The solid line represents recent (preliminary) data from Livermore[36], with error-bars omitted. The slightly higher theoretical value near I = 10^{16} W/cm² may be due to the 15% dump at critical being unrealistically high for the long pulse length of the experiment; a better fit would probably be obtained with a slightly higher value of f and a "dump-all" fraction smaller than 15%. In any case, the close agreement is highly suggestive that no additional mechanism such as SBS is responsible for the fall-off of the absorption with intensity.
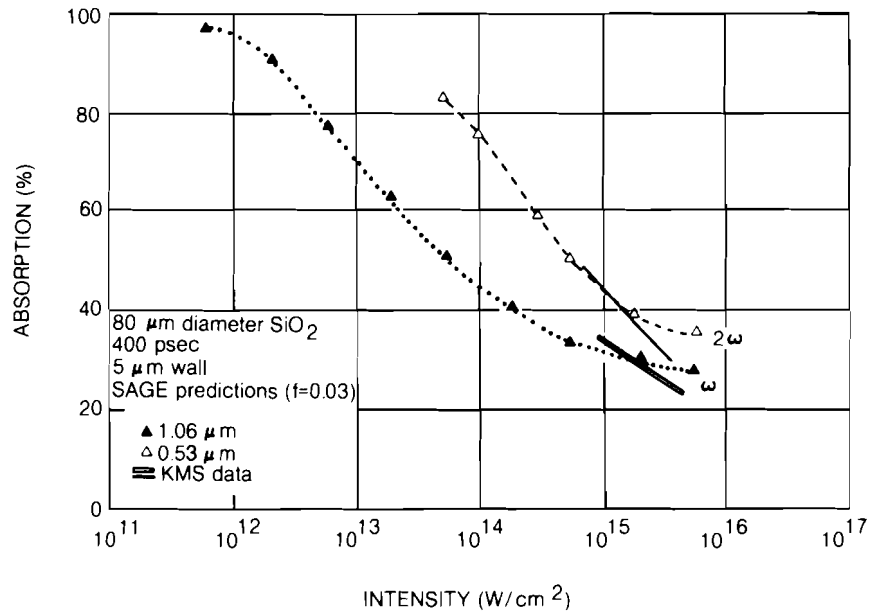
Figure 34

SAGE calculations of A(I) for f=0.03, for 400 psec pulses of 1.06μm and 0.53μm radiation on 80μm diameter glass shells with 5μm wall thickness. The solid lines are fits to recent KMS data[37].

We do not preclude the possibility that SBS might occur very close to the critical surface[41], when the scattered light would be subject to reabsorption in the plasma on its return path. In this case the total absorption would not be significantly degraded, although the small fraction "dumped" as resonant absorption would be reduced.

The $I\lambda^4$ scaling suggested by Equation 4 is also (approximately) illustrated in Figure 33. For example, the intensity at which 80% absorption is obtained scales with wavelength approximately as $I\lambda^{4.9}$.
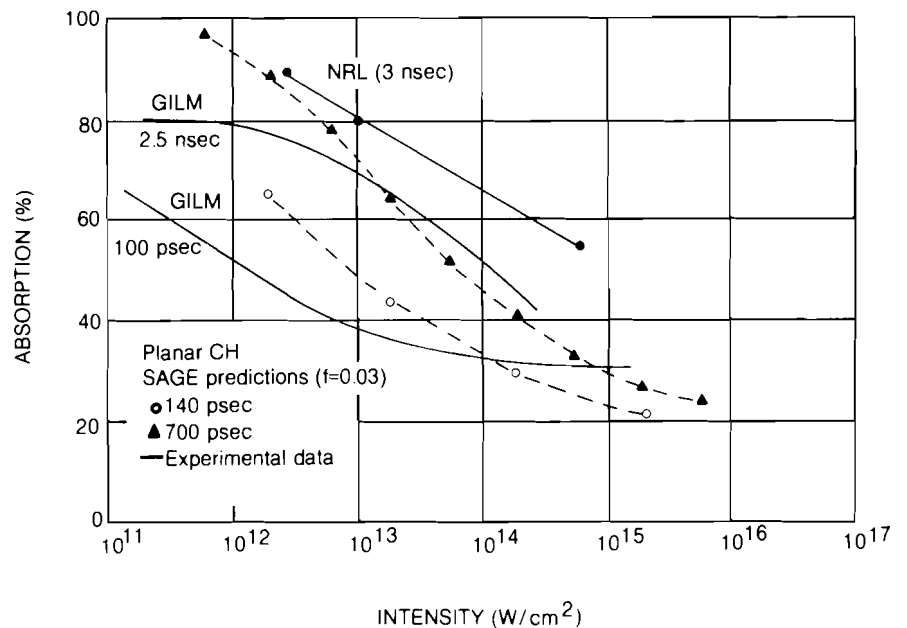

Figure 35

SAGE calculations of A(I) for f=0.03, for 140 and 700 psec pulses of 1.06μm radiation and planar CH targets. The solid curves represent recent GILM[38] and NRL[39] data obtained under slightly different conditions.

In Figure 34, we plot SAGE predictions for 80μm diameter glass microballoons irradiated by 400 psec pulses (triangles), together with recent KMS data[37] obtained under very similar conditions (solid lines). The experimental errorbars on absorption are typically $\pm$ 5% at 0.53μm and less at 1.05μm. Here again the calculations use f = 0.03. The comparison is close for both wavelengths, but again the 15% dump gives a theoretical overestimate of the absorption for intensities greater than a few times 10^{15} W/cm^2. The slope of the 0.53μm data is again consistent with the fall-off in absorption being entirely due to IB, and we note that the numerical model of SBS used by Slater et al.[37] predicts very little reflection due to SBS under these conditions. Our predictions in the 1.06μm case at high intensities are closer to experiment than one would expect because of our exclusion of ponderomotive steepening; the continued fall-off of the experimental data in Figure 32 suggests that resonance absorption is not very important at these 400 psec pulse lengths even for 1.06μm irradiation.

In Figure 35 we plot SAGE predictions for planar CH targets, together with GILM[38] and NRL[39] results for short and long pulses. Here we have not used exactly the same pulsewidths and focal spot sizes as in the experiments, and exact comparison is therefore impossible. However, the trends are basically in agreement. For the short pulse GILM experiment it is likely that the 15% resonant absorption fraction is an underestimate. We do not understand at present what causes the difference between the GILM and NRL data at longer pulsewidths.

Considerable interest has been generated by Amiranoff et al.[38] who observed absorptions of over 90% on planar CH targets at
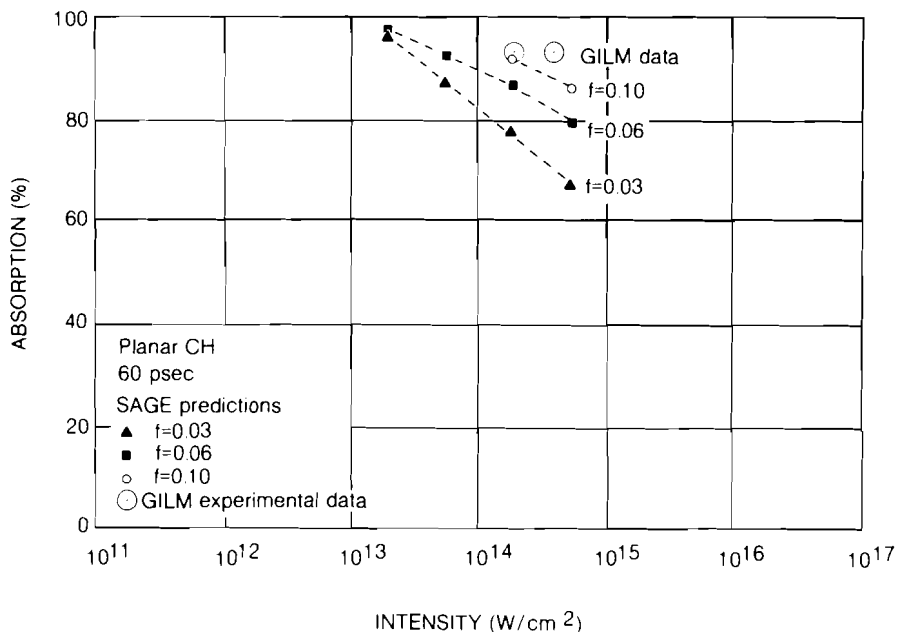
Figure 36

SAGE calculations of A(I) for 60 psec pulses of 0.26μm radiation on planar CH targets, for f=0.03, 0.06, and 0.10. Also shown are two recent GILM data points[38]

$I > 10^{14}$ W/cm² with 0.26μm radiation. These points, together with SAGE predictions for three different values of f, are shown in Figure 36. Here there is a definite discrepancy between theory and experiment, unless f is significantly greater than 0.03 in this case. Further experimental data, obtained over a broader intensity range, are clearly required.
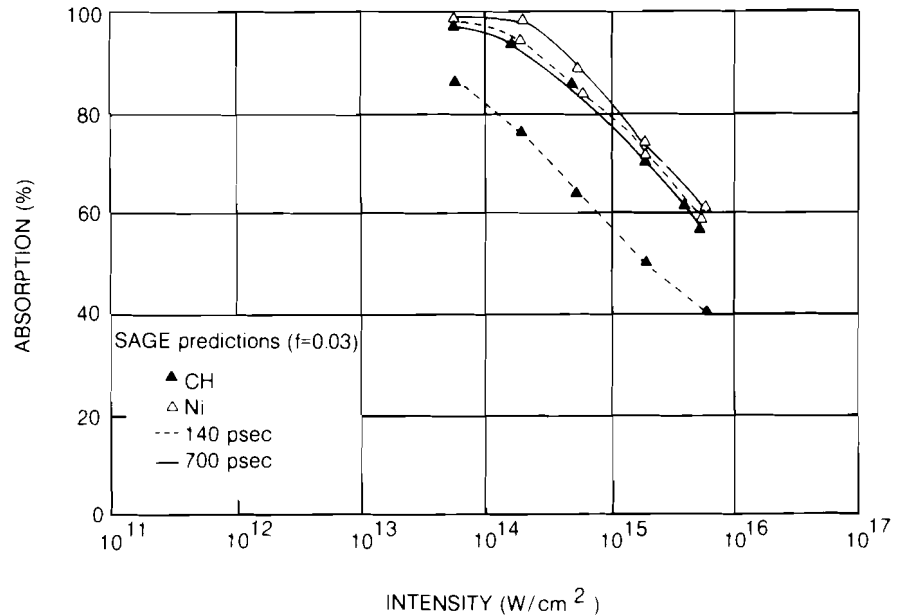
Figure 37

SAGE calculations of A(I) for f=0.03, for 140 and 700 psec pulses of 0.35μm radiation on planar CH and Ni targets.

Finally, Figure 37 gives SAGE predictions for the absorption of 0.35μm light for plastic and nickel, for long (700 psec) and short (140 psec) pulses. Again, a value of 0.03 is used for f. The two lower curves (solid triangles) show that for plastic the absorption increases significantly at longer pulses. The two upper curves (open triangles) suggest a surprising result that for nickel (Z=28) the absorption is almost independent of pulsewidth. This is believed to be due to a substantial steepening of the density profile near the critical density (induced by the low flux-limit parameter and not by ponderomotive forces which are not modeled).

It has recently been shown[40] that to correctly calculate the Doppler shift from a laser plasma two terms are involved, namely a shift ($2V_c/c$) associated with the velocity of the critical surface and an additional shift due to the change of plasma density n_e (and therefore refractive index μ) in the underdense region. The total shift is given by the rate of change of the total optical path-length:

$$\frac{\Delta\lambda}{\lambda} = \frac{d}{dt} \int \frac{\mu(x)dx}{c}$$

$$= \frac{d}{dt} 2\int_{x_c}^{\infty} \frac{1}{c} \sqrt{1 - n_e(x)/n_c} \, dx. \quad (5)$$

I > 10^{14} W/cm² with 0.26μm radiation. These points, together with SAGE predictions for three different values of f, are shown in Figure 36. Here there is a definite discrepancy between theory and experiment, unless f is significantly greater than 0.03 in this case. Further experimental data, obtained over a broader intensity range, are clearly required.
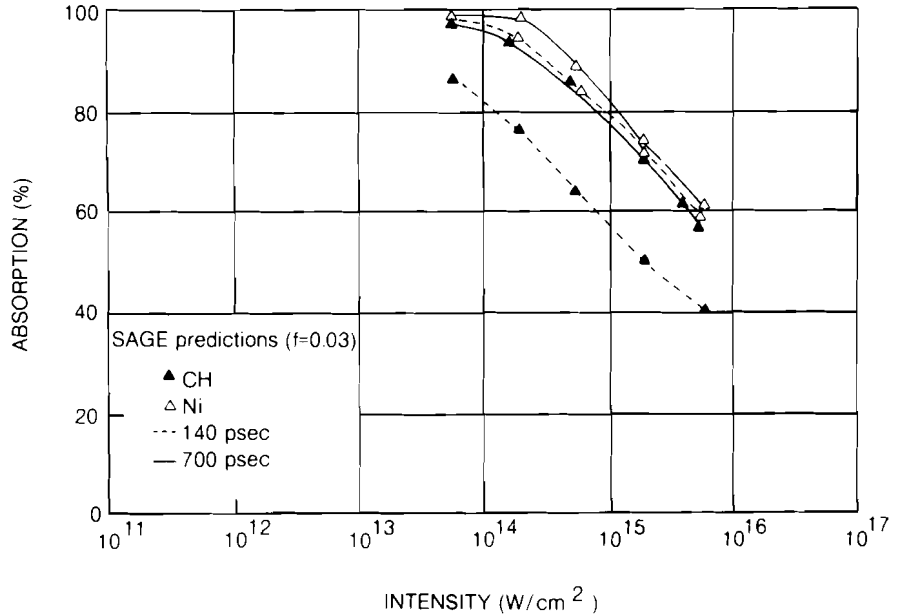
Figure 37

SAGE calculations of A(I) for f=0.03, for 140 and 700 psec pulses of 0.35μm radiation on planar CH and Ni targets.

Finally, Figure 37 gives SAGE predictions for the absorption of 0.35μm light for plastic and nickel, for long (700 psec) and short (140 psec) pulses. Again, a value of 0.03 is used for f. The two lower curves (solid triangles) show that for plastic the absorption increases significantly at longer pulses. The two upper curves (open triangles) suggest a surprising result that for nickel (Z=28) the absorption is almost independent of pulsewidth. This is believed to be due to a substantial steepening of the density profile near the critical density (induced by the low flux-limit parameter and not by ponderomotive forces which are not modeled).

It has recently been shown[40] that to correctly calculate the Doppler shift from a laser plasma two terms are involved, namely a shift ($2V_c/c$) associated with the velocity of the critical surface and an additional shift due to the change of plasma density n_e (and therefore refractive index μ) in the underdense region. The total shift is given by the rate of change of the total optical pathlength:

$$\frac{\Delta\lambda}{\lambda} = \frac{d}{dt} \int \frac{\mu(x)dx}{c}$$

$$= \frac{d}{dt} 2 \int_{x_c}^{\infty} \frac{1}{c} \sqrt{1 - n_e(x)/n_c} \; dx. \quad (5)$$

Figure 38

Predictions for the time history of the critical, half-, quarter- and eighth-critical surfaces for a 40μm thick CH slab irradiated by a 700 psec pulse of 0.53μm radiation at 1.5 × 10^14 W/cm². This calculation was performed in 2D.
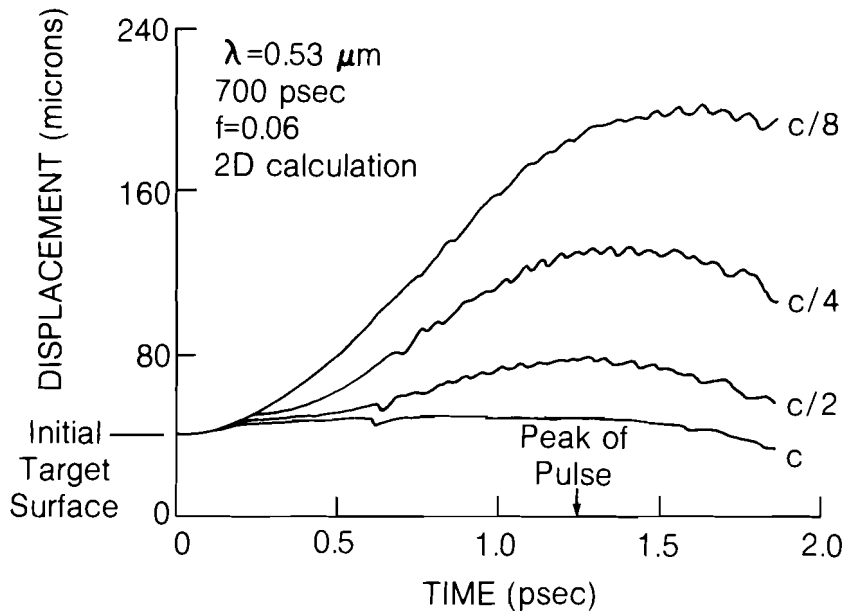
For example, for an exponential profile $n_e(x) = n_c \exp[(x_c-x)/L]$,

$$\frac{\Delta\lambda}{\lambda} = -\frac{2V_c}{c} - 1.23\,\frac{dL/dt}{c}\,. \qquad (6)$$

SAGE calculates the full shift given by Equation 5 for rays which are assumed to be reflected normally from the plasma. Both terms have been found to be important. A similar model has recently been implemented by Tarvin and Schroeder[42].
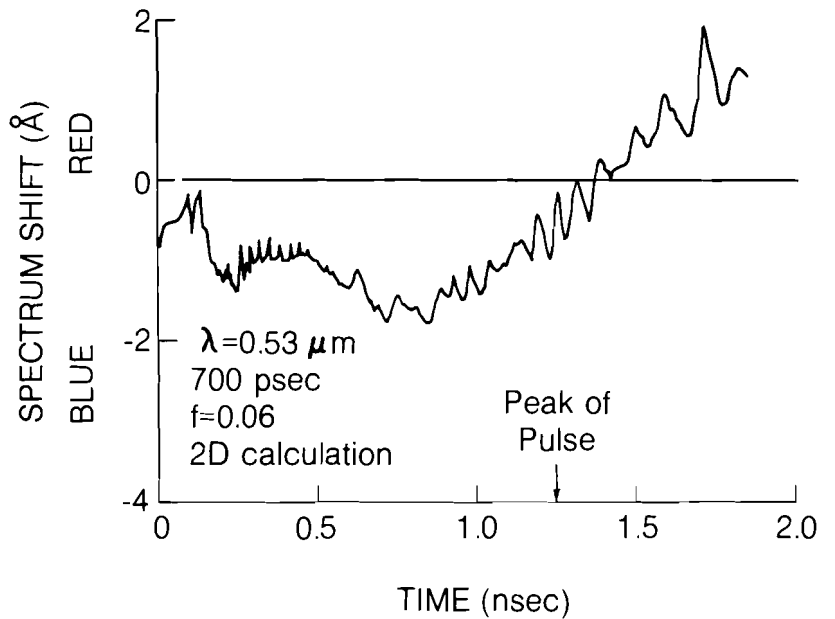

Figure 39

Predictions of the time history of the mean spectrum shift for the calculation of Figure 38.
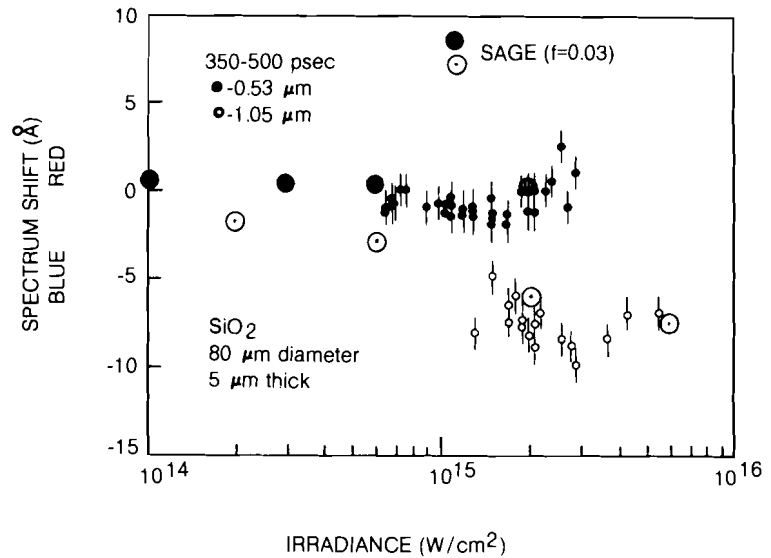
Figure 40

Predictions (circled points) for the time-integrated spectrum shift as a function of intensity, corresponding to the calculations of Figure 34, superposed on recent KMS experimental data[37].

In Figure 38 trajectories for the (on-axis) critical, half-, quarter- and eighth-critical surfaces are plotted for a 2D calculation of $0.53\mu m$ radiation incident upon a plastic target at 1.5×10^{14} W/cm^2. (In this example f= 0.06, but the same qualitative behavior obtains for other values of f.) The ripples on the curves are numerical artifacts which should be ignored. The critical surface initially moves out very slowly, and then stays steady over most of the pulse. The underdense plasma lengthscale, as may be estimated from the half-critical trajectory, increases up to the peak of the pulse, giving a blue-shift, and decreases later, leading eventually to a red-shift. A time history of the spectrum shift for this case would be as shown in Figure 39, where again it is the overall trend which is important while the ripples should be ignored.

The centroid of the time-integrated spectrum may also be calculated, and in Figure 40 we plot SAGE predictions (using f = 0.03) together with KMS experimental data[37] for 400 psec pulses. There is qualitative agreement in that there is no significant shift for $\lambda = 0.53\mu m$, but a significant blue-shift for $\lambda = 1.06\mu m$, varying weakly with intensity. The centroid shift is a difficult quantity to compare with experiment, as usually the width of the experimental spectrum is much greater than the shift[36]. The code does not predict this experimental broadening, which could be due to microscopic fluctuations in the plasma occurring on small time-scales or to possible SBS occurring very close to the critical surface as discussed above. However, it is arguable that the centroid shift represents the dominant average plasma motion. Even if the theory does not explain fully the backreflected spectrum, it is clear that an accurate calculation (and subtraction) of the Doppler shift must be made before drawing conclusions about SBS.

In summary, it has been shown that a large set of experimental absorption and backreflection data may be explained classically, in terms of "flux-limited" transport, without invoking additional physical processes such as Stimulated Brillouin Scattering. This does not show that these processes are unimportant[41], but rather underscores the need for the design of careful absorption experiments which resolve the important scattering and absorption processes.

Section 3
DEVELOPMENT IN
SUBPICOSECOND RESEARCH

3.A   A Simple Jitter-Free
Picosecond Streak Camera

The picosecond streak camera [43,44] is becoming a basic tool in
the study of optical transients in the picosecond time scale.
Other methods for accessing picosecond time resolution are
gated frequency mixing[45], optical Kerr shuttering[46], two-photon
fluorescence[47], and transient absorption spectroscopy[48]. In
many cases, use of a streak camera can lead to higher optical
sensitivity, time resolution, signal-to-noise ratio, and greater ease
in data taking. With the development of streak tubes with reso-
lution times of several picoseconds, the requirements for fast
high voltage switching has quickly increased. We have demon-
strated[49,50] for the first time that high voltage photoconductive
switching can exceed all these requirements and hence provide
an excellent streak camera driver. This section reports on a
recent further development in this area which greatly simplifies
the use of fast high voltage photoconductive switching applied
to the streak camera and results in a subpicosecond single-shot
jitter and unprecedented stability.

In order to achieve a time resolution of ~ 1 psec, a photoelectron
beam is swept at speeds approaching that of light across a
phosphor screen in the streak tube (image-convertor tube). This
requires an electrical ramp pulse of several kilovolts (1-5 kV)
synchronized with high accuracy to the event to be observed.
Conventional electronics can at best offer a jitter of ±50 psec for
short times with some long-term delay-drift. This comparatively

small jitter is obtained with avalanche transistor stacks which produce limited voltage ramps, leading to reduced sweep rates. The highest sweep rates previously obtained were achieved with optically-triggered spark gaps switching up to 16 kV, but with a jitter of several hundred picoseconds. At a large streak rate, this jitter is not tolerable.

A streak camera was operated with a light-activated silicon switch for the first time with a jitter of $\pm$ 1.7 psec [49,50] using a microsecond-length pulsed bias to avoid thermal instability [50,51]. It was pointed out that a major source of this jitter was the small fluctuations in switched voltage due to the statistical error in timing of the q-switched envelope from the oscillator with respect to the bias pulse which was only flat to within a few percent. In order to resolve this difficulty, a switch was biased at 2 kV DC and held at liquid nitrogen temperature in an evacuated vessel to avoid thermal instability [52,53,54]. Although this eliminates the need for a pulsed bias, several problems enter with the use of cryogenics. Intrinsic silicon has a dielectric breakdown field strength of $\sim 3 \times 10^5$ V/cm at room temperature and $\sim 10^2$ V/cm at liquid nitrogen temperature. This is attributed to a loss of electron-phonon scattering which increases the carrier mean-free-path in the absence of impurities. In order to circumvent this problem, deep impurity levels were added via doping with Au at $\sim 10^{15}$ cm^{-3}, thus providing sufficient impurity scattering to maintain a small mean-free-path and hence a large dielectric breakdown field strength. The addition of the Au limits the resistivity, and our experience was that a maximum of 3 kV DC could be held off by Au:Si at 77°K. To achieve large sweep rates, which enable the streak camera to operate at $\sim$1 psec resolution, larger voltages are needed. Also, the optical absorption coefficient of Si decreases as Si is cooled since at 1.06 μm the absorption is at the indirect edge (1.12 eV), and so the device becomes less sensitive ($\sim$6X) and can give voltage fluctuations which can lead to jitter in the streak camera. A further disadvantage of Au:Si is that the recombination time is only $\sim$ 50 nsec maximum. Contact heating becomes a problem at pulse lengths > 5 nsec, so a 3 nsec pulse was used. A room-temperature DC-biased switch would be preferable to this for a streak camera driver because of ease of operation, simplicity, portability and compactness.

To this end, GaAs:Cr was chosen because of its high resistivity ($\sim 10^8 \Omega$—cm) and hence large DC holdoff without thermal instability, and its high dielectric strength. A 3 mm gap is biased at 0-5 kV DC (Figure 41). When excited by a laser pulse (50-100 μJ @ 1.06 μm) the sample becomes conducting with a risetime limited by the laser pulsewidth [51], and returns to a non-conducting state after about 1.3 nsec (1/3). During this time, the deflection plates of an image convertor tube are charged through a current-limiting resistor R_C, and remain charged until bias resistor R_B returns the voltage to its initial value. With $R_B = 10^8$ Ω and $C_{plates} \cong 10^{-11}$F, this takes about 10^{-3} seconds. Thus, the
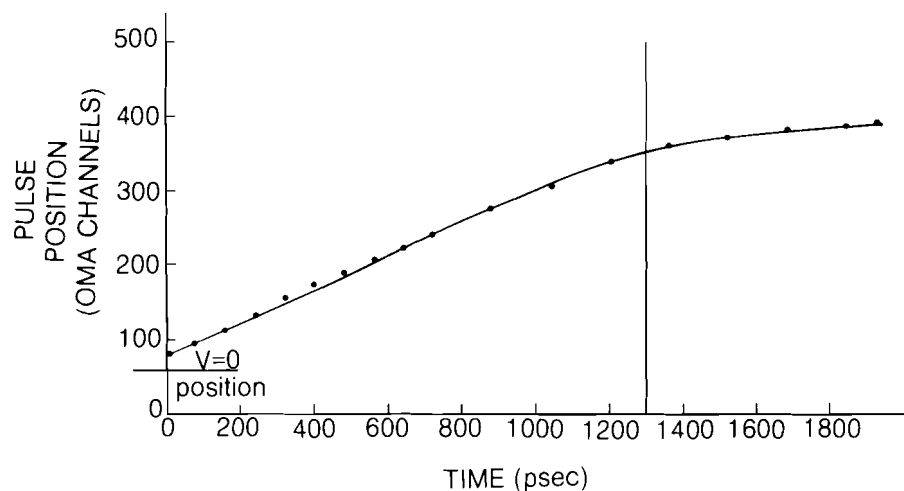
Figure 41

A single pulse is extracted with contrast ~10⁶ from a mode-locked Nd⁺³:YAG oscillator and frequency doubled and tripled for fluorescence kinetics studies. The remaining infrared energy (50-100μJ) is directed onto a 3 mm gap of GaAs doped with Cr which is DC-biased at 0-5 kV. Under the action of the laser pulse, the GaAs becomes conducting for 1.3 nsec and charges the deflection plates of the streak tube through a current-limiting, resistor R_C. The photo-electron beam is thus swept across the screen for 1.3 nsec and remains offscreen for ~ 1 msec while the plate offset bias resistor R_B discharges the plates. A short-cavity dye laser can be added to provide 10-15 psec pulses of selected wavelengths, and an OMA is used to collect and store the data.
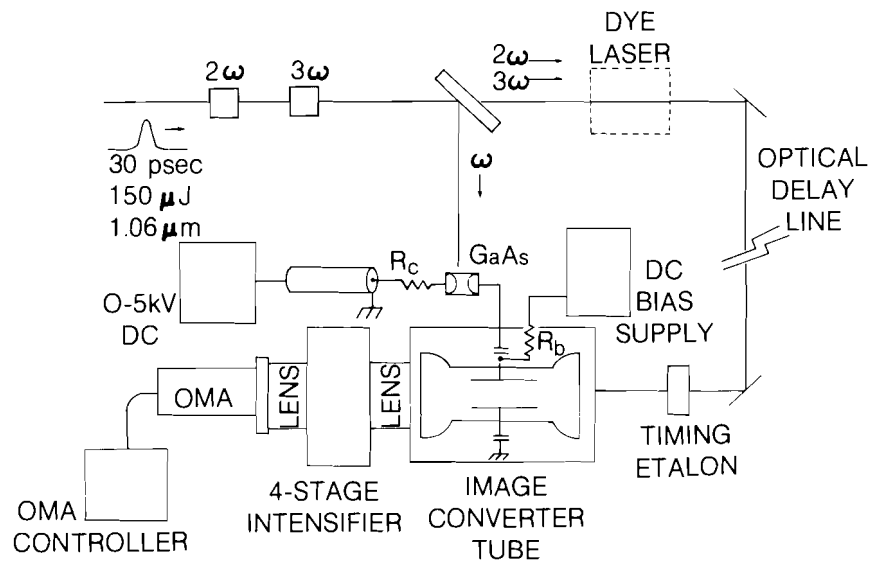
photoelectron beam is swept linearly over 1.3 nsec from off-screen on one side to off-screen on the other side, and the beam remains off the screen for a very large time compared to the fluorescence decay times of many systems. In many experiments, one is interested in studying emission risetimes on the scale of single picoseconds from samples which emit for times long compared to this (nsec to msec). In these experiments, the beam must remain deflected for up to msec. Long fluorescence decay times lead to problems in repetitively-scanned systems. Ramps of longer than 1.3 nsec can be obtained with a double-stage charging configuration.

Figure 42

Pulse peak position is plotted as a function of optical time delay in the signal line, showing a 2% linear ramp over 1.3 nsec. Longer ramp times can be obtained by using a two-stage charging. This data was taken with R_C=300Ω and V_{dc}=200 V.
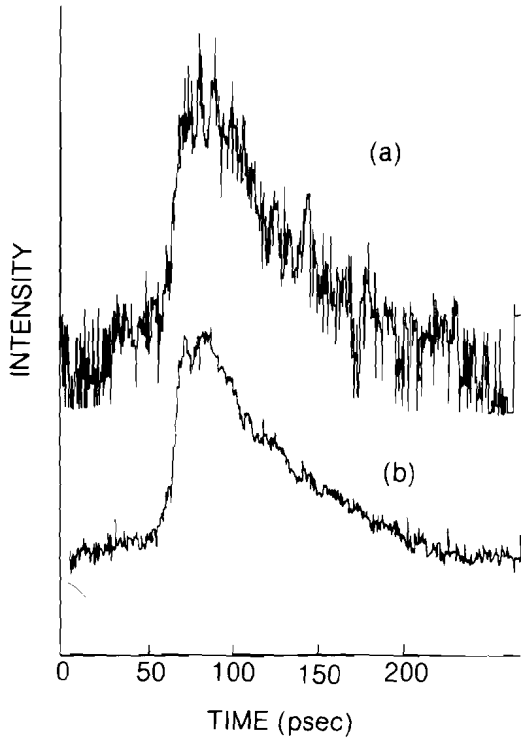
Figure 43

Fluorescence of Chlorophyll-A protein in leaf (a) 1 shot and (b) 20 shots accumulated. (Fluorescence attenuated to simulate small signal.) Signal-to-noise ratio is improved as the square root of the number of shots averaged.

Since the switching is purely photoconductive, good timing is expected compared to avalanche switching, and in this way, single-shot jitter is reduced to ± 0.8 psec at speeds of up to half the speed of light. The sweep speed is easily adjustable from 1 nsec full scale to 100 psec full scale by varying the DC bias voltage on the GaAs. Figure 42 shows the streak deflection function obtained

Figure 44
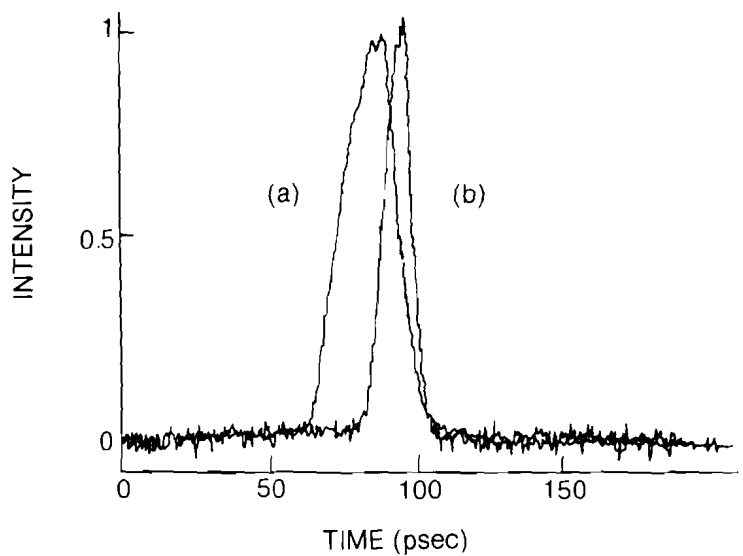
(a) Output at 580 nm from Rhodamine 6G in 500 μm wedged cavity with full (~20μJ) excitation energy in 30 psec and (b) output with input attenuated by ~30X. Note reduction in pulsewidth and time offset due to threshold of dye laser oscillation.

Figure 45

(a) Single shot of 14 psec dye laser pulse
(b) 20 shots of (a) accumulated
(c) single shot of Rose Bengal fluorescence, and
(d) 40 shots of (c) accumulated.
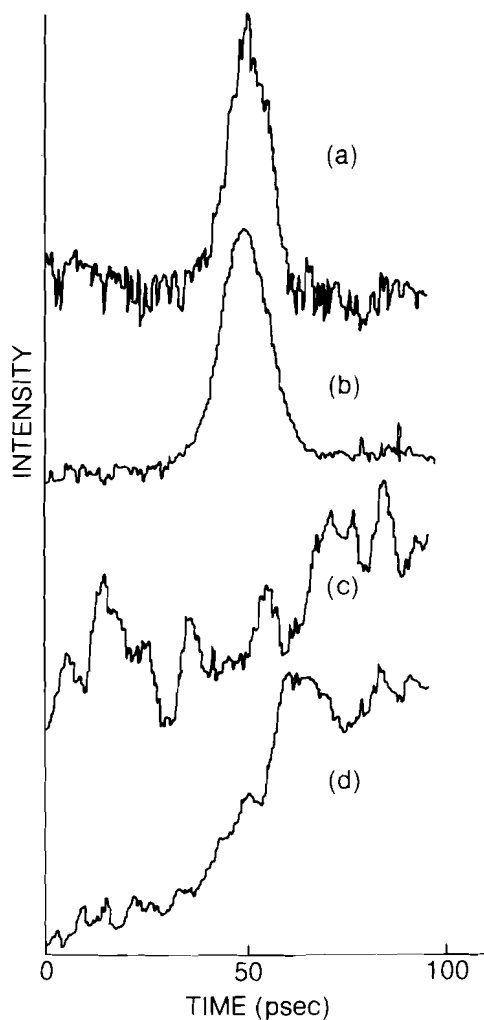
with R_C = 300 Ω and 2000 volts bias. Signal averaging can be performed with this low jitter to increase further the available timing precision and signal-to-noise ratio. Figure 43 shows the effect of averaging an attenuated fluorescence signal to simulate low quantum yield.

To increase the versatility of the system, a wedged short-cavity dye laser was added (Figure 41) which when pumped with a single green pulse (530 nm) produces a 10-25 psec pulse of wavelength determined by the choice of the dye. The pulsewidth obtained is determined by the pump intensity. With an incident energy of ~ 20 μJ, the dye laser is pumped far above threshold and gives stable pulses of ~ 25 psec (Figure 44a). At 30 times less pump intensity, pulses of 10-15 psec are obtained (Figure 44b). A time offset of 12 psec is observed which is due to the thresholding effect of the dye laser. The effect of short-pulse signal averaging is demonstrated in Figure 45. A single dye pulse (R6G) at 580 nm is shown with one and twenty shots accumulated. This pulse is then used to excite Rose Bengal dye in water (~10^{-4}M) and the

fluorescence output is shown with one shot and 40 shots accumulated. A large increase in signal-to-noise ratio is observed. The single-shot data is virtually unintelligible, whereas the averaged data has fairly good signal-to-noise ratio.

The use of a simple room-temperature DC-biased photo-conductive switch has been shown to increase the performance of a streak camera in timing stability ($\pm$0.8 psec jitter), sweep speed (~½ speed of light) and ease of operation (no pulsed-bias, vacuum, liquid nitrogen, etc.). Voltage fluctuations (sweep speed fluctuations) were controlled to less than $\pm$ 0.1%, resulting in exceptional stability and reliability, and the system has no short- or long-term drift. This permits averaging experiments to extend over long periods of time to gain timing accuracy into the femtosecond domain and large signal-to-noise ratios for detailed fluorescence studies. Single-shot averaging has many advantages over repetitively scanned systems.

It is emphasized that with this technique in many cases the complex, unreliable, and cumbersome electronics commonly used with streak cameras can be replaced with an inexpensive, simple, and highly accurate device capable of increasing the usefulness of the streak camera tremendously.

The addition of a wedged short-cavity dye laser provides short pulses of numerous wavelengths across the visible spectrum for use in time-resolved emission studies.

It should be mentioned that the performance of this system in terms of timing accuracy scales with the laser pulsewidth used to excite the GaAs. With the use of a gigawatt subpicosecond source currently under construction at LLE, the expected timing accuracy is less than 0.1 ps.

3.B Picosecond Microwave Pulse-generation

Short optical pulses have been used in the past, in conjunction with bulk semiconductors to switch[55,56] and phase shift [57] microwave signals. Here we report the generation of picosecond microwave bursts inherently synchronized with an optical trigger pulse by shock excitation of an X-band waveguide. The excitation is generated by a high-voltage photoconductive switch driven by a picosecond optical pulse. This fast switching technique[58] provides a means of generating a high-voltage pulse in picosecond synchronism with the optical driving pulse. This high-voltage switching technique developed and implemented in the laser-

Figure 46

A laser-induced photoconductive switch is coupled to an X-band waveguide. The microwave burst is sent to an X-band dish-type antenna. The signal reflected back from the target is fed to a crystal detector by means of a circulator.
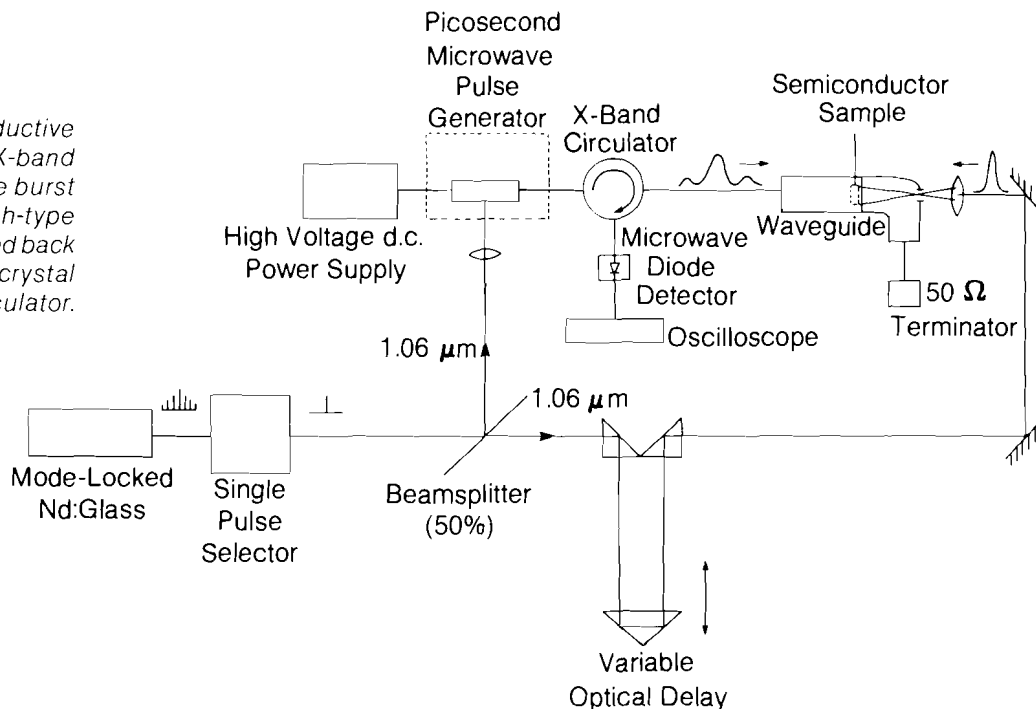
driven fusion area[59,60,61] now finds a new application in picosecond microwave pulse generation. A measured pulse duration of 50 psec, corresponding to the optical excitation pulsewidth, has been obtained. Shorter pulses can be achieved by using picosecond or subpicosecond optical excitation.

The concept of producing microwave radiation by means of "shock" excitation of a transmission line is not new[62,63]. In the past, microwave pulses have been created in the subnanosecond time domain by electrically driven spark gaps. Because this switching mechanism relies on avalanche multiplication, this technique is limited to lower microwave frequencies and is affected by switching time fluctuations. In addition, laser-activated photoconductive switching has been used to generate rf pulses, for example, with the frozen-wave generator[64]. Microwave frequencies were not attained due to the long laser pulsewidth. The present effort combines some of the features of these previously reported results. The microwave pulsewidth has been determined by a gating technique based on the change of reflectivity induced in a slab of Ge by the short optical pulse. The microwave pulse duration has been found to be less than 50 psec, in good agreement with the laser pulsewidth. The peak microwave power in the burst has been estimated to be on the order of 100 MW and is sufficient to allow a high-resolution radar experiment to be performed.

A schematic representation of the microwave generator is shown in Figure 46. A piece of semi-insulating Cr-doped GaAs

interrupts the center conductor of a coaxial line and is biased by a high-voltage DC power supply[59]. The switching action is initiated by laser-induced photoconductivity in the semiconductor crystal. The optical driving pulse is generated by a Nd^{+3}: YAG laser, actively and passively mode locked. The laser wavelength is centered around 1.064μm and the pulse duration is 35± 5 psec. For a bias voltage of a few hundred volts, 10 μJ of absorbed optical energy is required to achieve good switching efficiency. In a wideband geometry the electrical pulse exhibits a risetime dictated by the laser pulse width, i.e. 35 ± 5 psec. The fall time is determined by charge line length and by the carrier recovery time, which is Cr-concentration dependent. The switch drives an X-band coaxial line-to-waveguide transition. The transition is modified by removal of the rear wall. This nearly eliminates the microwave reflection from the end of the waveguide and aids in reducing the microwave pulsewidth. The transition is then no longer matched, in the conventional sense, to the coaxial input. Upon laser action, the charge stored in the charge line is dumped into the transition, resulting in an RF emission. The microwave burst is guided via WR-90 waveguide to a 20 dB broadband ferrite circulator and then to an X-band dish-type antenna. The signal reflected from a target is received by the same antenna and circulated back to a standard microwave crystal detector located on the third port of the circulator. The crystal detector has a response time FWHM of 500 psec. The target is a flat aluminum plate located about 4m from the antenna. Figure 47 shows two echoes separated by about 500 psec obtained for two target positions differing by 8 cm. The spatial resolution is ultimately limited by the oscilloscope trace width and corresponds here to a few millimeters.
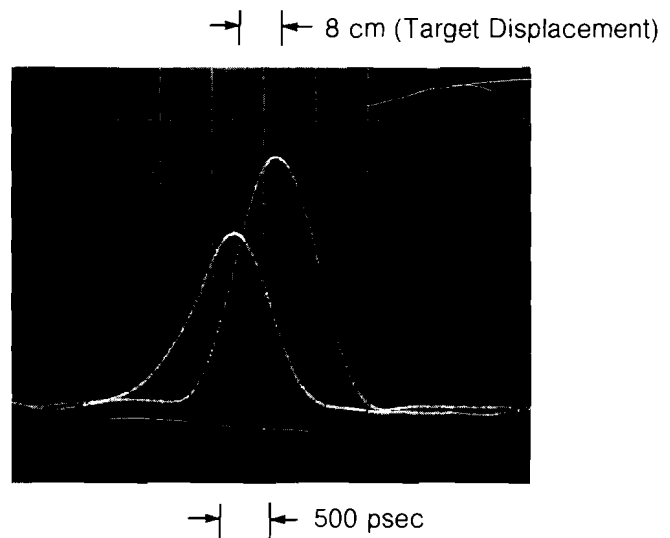

Figure 47

Oscilloscope display showing the detector output for two target positions 8 cm apart from a target located 4m away from the microwave dish.

Figure 48

The microwave burst generated by a GaAs switch activated by a 30 psec, 1.06μm optical pulse coming from Nd:YAG mode locked laser, is gated by laser-induced reflectivity in a Ge wafer. The microwave reflectivity of the Ge is measured as a function of the time delay between the micro- wave and the optical bursts. The carrier recovery time in Ge is several microseconds so the time integral of the microwave burst can be generated.
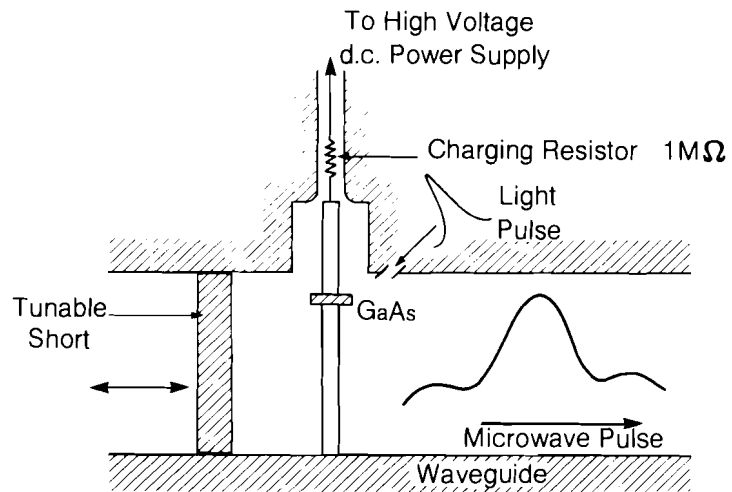
CHARACTERISTICS
- Optically synchronized picosecond microwave burst
- 100 GHz obtainable with subpicosecond optical pulse

The electronic system, consisting of the oscilloscope and detector, has a combined bandwidth on the order of 1 GHz and is inadequate to time resolve the microwave burst. This difficulty was overcome by using a gating technique illustrated in Figure 48 and taking advantage of the synchronism between the microwave and optical pulses. The microwave burst is reflected by a laser-induced electron-hole plasma in a thin wafer of intrinsic germanium mounted across the waveguide. (The wafer is made thin (50μm) to reduce microwave reflections due to intrinsic carriers and dielectric mismatch but is still substantially thicker than the optical penetration depth of about 2μm in order to maximize optical carrier generation and provide mechanical support.) The time delay between the illumination of the Ge sample and the microwave burst can be varied over several hundreds of picoseconds by means of an adjustable optical delay line. In the absence of illumination, the Ge is nearly transparent to microwaves and reflects only 1% of the incident wave. The transmitted pulse is absorbed in a matched load. If the microwave burst arrives at the semiconductor sample shortly after illumination, the microwave pulse is readily reflected by the laser induced electron hole plasma. For an incident optical energy of 500 μJ absorbed in the thin slab and spread over 1 cm², roughly 30% of the incident microwave power is reflected. The reflected signal is integrated by the detection system (detector-oscilloscope). The detector output pulse height, as observed on the oscilloscope, is plotted as a function of the time delay between the microwave and optical bursts and is illustrated in Figure 49. Due to the relatively long carrier lifetime in Ge (on the order of microseconds) the plasma reflectivity is sustained long after the illumination ceases. Therefore the resulting microwave reflection is a microwave burst truncated by the step function of

the Ge reflectivity and represents the time integral of the signal. From a knowledge of the laser pulse duration, a FWHM of less than 50 psec can be determined for the microwave burst. This result is in good agreement with the laser pulsewidth and the waveguide cut-off frequency of 6.56 GHz which establish, respectively, the upper and lower frequency boundaries of the microwave spectrum generated.

We have shown that microwave bursts in picosecond synchronism with an optical pulse may be generated using a laser-activated photoconductive switch coupled to an X-band waveguide. A 50 psec microwave pulse was generated using a 35 ± 5 psec optical trigger pulse. Further efforts to determine the microwave power as well as the spectral content are underway. Current efforts also involve extension of this technique to the millimeter wave range by using picosecond or subpicosecond optical pulses. An application of short microwave pulses is illustrated in this section with a high-resolution radar experiment. Potential applications of these bursts are many and include studies pertaining to electron-hole plasma kinetics, plasmas associated with laser-driven fusion, temporal investigation of the surface properties of semi-conductors undergoing laser annealing, and light-matter interactions such as in biological materials or photographic emulsions.
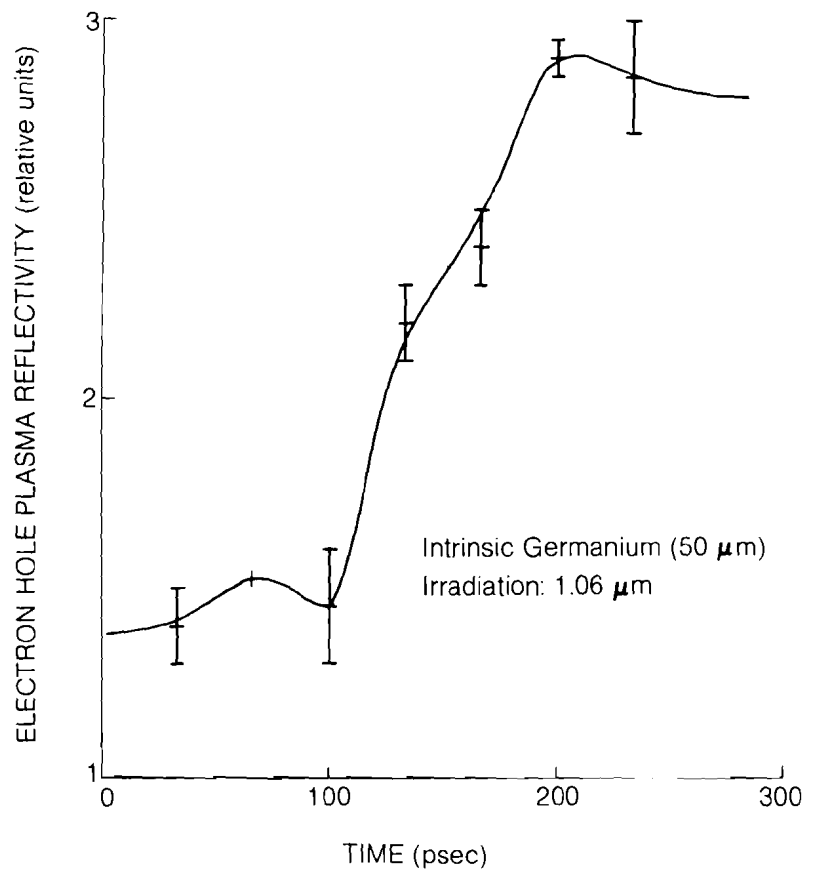

Figure 49

The derivative of the signal unfolded with the laser pulsewidth leads to an upper limit of the microwave pulse of 50 psec.

Section 4
NATIONAL LASER USERS
FACILITY NEWS

During the past quarter, the Department of Energy issued its first user contract to Professor Lawrence Knight of Brigham Young University, Provo, Utah. Professor Knight will be testing novel optics for use in the x-ray region, including the use of synthetic crystals in an x-ray spectrometer. Drawings of the apparatus that Professor Knight will use were received at LLE in late August for verification that the experiment is compatible with its proposed location on the OMEGA target chamber. The experiment is scheduled for check-out shots in January, with further shots later in 1981.

In August, the Department of Energy issued a Notice of Program Interest stating its interest in receiving unsolicited proposals for experiments that could be performed at the National Laser Users Facility. The notice contains the details of information that should be included in the proposal. Copies of the notice can be obtained from Dr. Jack Wilson at the Laboratory for Laser Energetics, or from Mr. Rex Purcell, D.O.E. Nevada Operations Office P.O. Box 14100, Las Vegas, Nevada, 89114. Proposals should be sent to Mr. Purcell.

In Volume 1 of LLE Review there was a brief description of a workshop held at LLE last November to explore possible experiments using very high power lasers in areas other than laser fusion. A complete report of that workshop has now been produced and is available from Dr. Jack Wilson.

AMONG OUR VISITORS

Federal and state government officials spent an afternoon at the Laboratory in August and expressed great interest in the facilities and the research program in laser fusion. The distinguished visitors were accompanied by Dr. Robert Sproull, President of the University, and were taken on a tour of the facility by the Director.

The distinguished visitors included Governor Hugh Carey, Senator Ernest F. Hollings (South Carolina), Senator Daniel Inouye (Hawaii), Senator Silvio Conte (Massachusetts), and U.S. Senate Sergeant at Arms, F. Nordy Hoffman.

Figure 50 *A few of the distinguished visitors to LLE discuss the laboratory's programs with the Director. Left to right: Senator Ernest F. Hollings (South Carolina); Senator Daniel Inouye (Hawaii); Moshe J. Lubin, Director of LLE; Governor Hugh Carey; Mrs. Inouye; Donald K. Hess, Vice President for Campus Affairs; and University of Rochester President Robert L. Sproull.*

PUBLICATIONS AND CONFERENCE PRESENTATIONS

Publications

1. "High-Density Effects on Thermonuclear Ignition for Inertially Confined Fusion," S. Skupsky; *Phys. Rev. Lett.,* **44,** 26 (June 1980), pp. 1760-63.

2. "Soft X-Ray Population Inversion in Laser Plasmas by Resonant Photoexcitation and Photon-Assisted Processes," V. A. Bhagavatula; *IEEE Journal of Quantum Electronics* **QE-16,** 6 (June 1980), pp. 603-18.

3. "X-Ray Absorption Lines: Signature for Preheat Level in Non-Explosive Laser Implosions," B. Yaakobi, R. L. McCrory, S. Skupsky, J. A. Delettrez, P. Bourke, H. Deckman, C. F. Hooper, and J. M. Soures; *Optics Communications,* **34,** 2 (August 1980), pp. 213-17.

4. "Electro-Optic Prepulse Suppression for Fusion Laser Systems," G. Mourou, J. Bunkenburg and W. Seka; *Optics Communications,* **34,** 2 (August 1980), pp. 252-54.

Forthcoming Publications

"Laser Fusion Breeder Fueled Electricity Generation Systems," David H. Berwald, James Maniscalco; submitted for publication in *Nuclear Technology.*

"An Economics Method for Symbiotic Fusion-Fission Electricity," David H. Berwald, James A. Maniscalco; submitted for publication in *Nuclear Technology*.

"Design and Performance Characteristics of High Power Phosphate Glass Laser System," W. Seka, J. Soures, O. Lewis, J. Bunkenburg, D. Brown, S. Jacobs, G. Mourou, J. Zimmerman; accepted for publication by *Applied Optics*.

"Spectral Methods for Multi-Dimensional Diffusion Problems," R. L. McCrory, S. A. Orszag; accepted for publication by *Journal of Computational Physics*.

"A Simple Silicon Switch-Driven Psec Streak Camera," W. Knox, W. Friedman, G. Mourou; accepted for publication by *Applied Physics Letters*.

"Two-Dimensional Calculations of Non-Spherical Laser Fusion Implosions," R. S. Craxton and R. L. McCrory; submitted for publication in *Nuclear Fusion*.

"Laser Cross Linking of RNA Polymerase and DNA," Catherine A. Harrison, Douglas H. Turner, Jack Wilson, Mark A. DeWyngaert, and David C. Hinkle; submitted for publication in *Journal of American Chemical Society*.

"X-Ray Absorption Fine Structure Measurement Using Laser Compressed Target as a Source," B. Yaakobi, H. Deckman, P. Bourke, S. Letzring, J. M. Soures; accepted for publication by *Applied Physics Letters*.

"Time Resolved Spectroscopy of Large Bore Xe Flashlamps for Use in Large Aperture Amplifiers," John H. Kelly, David C. Brown, and Kenneth Teegarden; accepted for publication by *Applied Optics*.

"Theory of High Efficiency Third Harmonic Generation of High Power Nd: Glass Laser Radiation," R. S. Craxton; accepted for publication by *Optics Communications*.

"Demonstration of High Efficiency Third Harmonic Conversion of High Power Nd:Glass Laser Radiation," W. Seka, S. D. Jacobs, J. E. Rizzo, R. Boni, R. S. Craxton; accepted for publication by *Optics Communications*.

"Picosecond Switching of a Multi-Kilovolt DC Bias with Laser Activated Silicon at Low Temperature," Michael Stavola, Mark G. Sceats, Gerard Mourou; accepted for publication by *Optics Communications*.

"Picosecond Time Delay Fluorimetry Using a Streak Camera," Michael Stavola, Gerard Mourou, Wayne Knox; accepted for publication by *Optics Communications*.

Conference Presentations

1. "Synchronization of a Mode-Locked Nd:YAG-Argon Ion Laser System," G. T. Harvey, C. W. Gabel, and G. Mourou; Optical Society of America Topical Meeting on Picosecond

Phenomena, North Falmouth, Massachusetts, June 17-20, 1980.

2. "Alignment System Devices for Medium Repetition Rate Glass Fusion Laser," J. F. Hoose; Society of Photo-Optical Instrumentation Engineers Technical Symposium, San Diego, California, July 28 – August 1.

REFERENCES

1. G. Birkhoff, *Relativity and Modern Physics,* (Harvard University Press, Cambridge, Mass., 1923) p. 253.

2. J.L.Synge, *Relativity – The General Theory,* (North-Holland, Amsterdam, 1964) p. 276.

3. J. D. Jackson, *Classical Electrodynamics,* (2nd ed., John Wiley & Sons, New York, 1975), ch. 16.

4. J. D. Jackson, op. cit., ch. 9.

5. M. Born and E. Wolf, *Principles of Optics,* (5th ed., Pergamon Press, London, 1975) ch. 10; L. Mandel and E. Wolf, *Rev. Mod. Phys.,* **37**, 231 (1965). An easier version can be found in M. V. Klein, *Optics,* (John Wiley & Sons, New York, 1970) ch. 6.

6. A. Marechal, in *Symposium on Optical Image Evaluation,* 1 (National Bureau of Standards Circular 526, 1954) p. 9.

7. W. K. H. Panofsky and M. Phillips, *Classical Electricity and Magnetism,* (2nd ed., Addison-Wesley, Reading, Mass., 1962), ch. 13; M. Born and E. Wolf, Section 13.5; P. J. Wyatt, *Phys. Rev.* **127**, 1837 (1962).

8. J. H. Erkkila, Ph.D. Dissertation (University of California, Livermore, 1975).

9. H. H. Hopkins, *Proc. Phys. Soc.* (London) **55**, 116 (1943).

10. B. Richard and E. Wolf, *Proc. Phys. Soc.* (London), **B69**, 854 (1956); *Proc. Roy. Soc.* (London), **253A**, 358 (1959); E. Wolf, ibid. **253A**, 349 (1959).

11. G. Leppelmeier, *Experimental Planning Group Technical Report 9*, LLE, (1976).

12. K. Lee, *LLE Lab. Report 88*, (1979).

13. J. E. Howard, University of Wisconsin, Fusion Technology Program, VWFDM-172, 1976.

14. R. E. Kidder, *Nucl. Fusion*, **16**, 3(1976); J. D. Lindl and W. C. Mead, *Phys. Rev. Lett.*, **34**, 1273 (1975); R. L. McCrory, R. L. Morse, and K. A. Taggart, *Nucl. Sci. Eng.*, **64** 163 (1977).

15. R. J. Faehl and W. L. Kruer, *Phys. Fluids*, **20**, 55 (1977); W. M. Manheimer, *Phys. Fluids*, **20**, 265 (1977).

16. W. M. Manheimer and D. G. Colombant, *Phys. Fluids*, **21**, 1818 (1978).

17. J. W. Shearer, *Phys. Fluids*, **14**, 183 (1971); I Fidoue, N. Cimento, **30**, 666 (1963).

18. R. C. Malone and R. L. Morse, *LASL Report LA-6446-MS*, (1976); *Phys. Fluids*, **21**, 143 (1978).

19. E. I. Thorsos, T. C. Bristow, J. A. Delettrez, J. M. Soures, and J. E. Rizzo, *Appl. Phys. Letter*, **35**, 598 (1979).

20. R. E. Turner, L. M. Goldman, *Phys. Rev. Lett.*, **44**, 400 (1980).

21. W. Seka, J. Soures, O. Lewis, J. Bunkenberg, D. Brown, G. Mourou, J. Zimmerman, *Appl. Opt.*, **19**, 409 (1980).

22. S. Sarraf, L. M. Goldman, to be published; E. Thorsos (editor), *LLE Review, Vol II*, Figure 10 (unpublished).

23. R. Turner, *LLE Lab. Report 105*, (1980), (unpublished).

24. C. S. Liu, M. N. Rosenbluth, R. B. White, *Phys. Fluids*, **17**, 1211 (1974).

25. L. M. Gorbunov, A. N. Polyanichev, *Sov. J. Plasma Phys.* **5**(3), 316 (1979).

26. L. M. Goldman, J. Soures, M. J. Lubin, *Phys. Rev. Lett.*, **31**, 1184 (1973).

27. A. Ng, L. Pitt, D. Saltzmann, A. A. Offenberger, *Phys. Rev. Lett.* **42**, 307 (1978).

28. M. J. Herbst, C. E. Clayton, F. F. Chen, *Phys. Rev. Lett.*, **43**, 1591 (1979).

29. R. S. Craxton and R. L. McCrory, *LLE Lab. Report 99*, (1980).

30. K. Estabrook and W. L. Kruer, *Phys. Rev. Lett.* **40**, 42 (1978).

31. W. L. Kruer, R. A. Haas, W. C. Mead, D. W. Phillion and V. C. Rupert in *Plasma Physics*, ed. H. Wilhelmsson. Plenum, New York (1977), p. 64.

32. R. C. Malone, R. L. McCrory and R. L. Morse, *Phys. Rev. Lett.*, **34**, 721 (1975).

33. B. I. Bennett, J. D. Johnson, G. I. Kerley and G. T. Rood, *Los Alamos Report LA-7130*, (1978).

34. W. F. Huebner, A. L. Merts, N. H. Magee, and M. F. Argo, *Los Alamos Report LA-6760-M,* (1977).

35. A. B. Langdon, *Phys. Rev. Lett.,* **44,** 575 (1980).

36. E. M. Campbell, V. C. Rupert, W. C. Mead, R. E. Turner, C. E. Max, K. G. Estabrook, *14th European Conference on Laser Interaction with Matter,* Palaiseau, France (Sept. 1980); and E. M. Campbell, private communication.

37. D. C. Slater, R. L. Berger, Gar. E. Busch, G. Charatis, R. R. Johnson, F. J. Mayer, D. Mitrovich, R. J. Schroeder, J. D. Simpson, D. Sullivan, D. J. Tanner and J. A. Tarvin, to be published in *8th International Conference on Plasma Physics and Controlled Nuclear Fusion Research,* I.A.E.A., Vienna (1980).

38. F. Amiranoff, R. Benattar, R. Fabbro, E. Fabre, C. Garban, C. Popovics, J. Virmont and M. Weinfeld. (a) *Bull. Amer. Phys. Soc.,* **24,** 1069 (1979), and (b) Rapport d' Activite 1979 Du Groupement de Recherches Coordonnees Interaction Laser-Matiere (GILM), Centre National de la Recherche Scientifique (Ecole Polytechnique-91128 Palaiseau Cedex) (1980), pp. 64-75.

39. B. H. Ripin, S. E. Bodner, S. H. Gold, R. H. Lehmberg, E. A. McLean, J. M. McMahon, S. P. Obenschain, J. A. Stamper, R. R. Whitelock, F. C. Young, H. R. Grien, J. Grun and M. J. Herbst, *NRL Memorandum Report,* **4212,** (1980).

40. T. Dewandre, J. R. Albritton and E. A. Williams. Laboratory for Laser Energetics, University of Rochester (unpublished). Submitted to *Phys. Fluids,* (1980).

41. K. Estabrook, private communication.

42. J. A. Tarvin and R. J. Schroeder, *KMS Fusion Report,* KMS-U 1033 (1980).

43. N. H. Schiller, Y. Tsuchiya, E. Inuzuka, Y. Suzuki, K. Kinoshita, K. Kamiya, H. Lida and R. R. Alfano in *Optical Spectra,* June, (1980). p. 55 gives a good introduction to the streak camera.

44. D. J. Bradley and G. H. C. New, *Proc. IEEE,* **62,** 313 (1974), and D. J. Bradley, *Opt. Laser Tech.,* Feb. (1979).

45. B. Kopainsky and W. Kaiser, *Opt. Comm.,* **26,** 219 (1978).

46. M. A. Duguay and J. W. Hansen, *Appl. Phys. Lett.,* **15,** 192 (1969).

47. D. Von Der Linde, *IEEE Journal of Quantum Electronics* **QE-8,** 328, (1972).

48. R. W. Anderson, D. E. Damshen, G. W. Scott and L. B. Talley, *J. Chem Phys.,* **71,** 1134 (1979).

49. W. Knox, W. D. Friedman and G. Mourou, Post Deadline Paper I-2, CLEA Washington, D.C. (May, 1979).

50. G. Mourou and W. Knox, *Appl. Phys. Lett.,* **36,** 623, (1980).

51. G. Mourou and W. Knox, *Appl. Phys. Lett.,* **35,** 492, (1979).

52. M. Stavola, G. Mourou and M. Sceats, *Opt. Comm.,* (submitted).

53. M. Stavola, G. Mourou and W. Knox, *Opt. Comm.*, (submitted).

54. R. Frankel, G. Mourou, W. Knox and M. Stavola, *Nature,* (submitted).

55. A. M. Johnson and D. H. Auston, *IEEE Quantum Electronics,* vol. **QE-11**, 283 (1975).

56. C. H. Lee, P. Mak and A. P. DeFonzo, *IEEE Quantum Electronics,* vol. **QE-16**, 277 (1980).

57. A. P. DeFonzo, C. H. Lee and P. S. Mak, *Appl. Phys. Lett.,* **35**, 575 (1979).

58. D. H. Auston, *Appl. Phys. Lett.,* **26**, 101 (1975).

59. G. Mourou and W. Knox, *Appl. Phys. Lett.,* **35**, 492 (1979).

60. J. Agostinelli, G. Mourou and C. Gabel, *Appl. Phys. Lett.,* **35**, 731 (1979).

61. G. Mourou and W. Knox, *Appl. Phys. Lett.,* **36**, 623 (1980).

62. J. M. Proud, Jr. "Radio Frequency Generators", U.S. Patent 3484619, Dec. 16, (1969).

63. V. M. Ristic and T. P. Sorensen, *IEEE Trans. Microwave Theory Tech.,* vol. **26**, (May, 1978), pp. 369-374.

64. J. M. Proud, Jr. and S. L. Norman, *IEEE Trans. Microwave Theory Tech.,* vol. **MTT-26**, (Mar. 1978), pp. 137-140.